4

CHAPTER 4: NUMERICAL OPTIMISATION OF OPERATING AND DESIGN PARAMETERS FOR A PEM FUEL CELL

4.1 INTRODUCTION

Fuel cell technology is rapidly advancing due to the need for high energy efficiency and low environmental impact. Fuel cells are regarded as a potential reliable future source of energy supply due to the fact that they are one of the cleanest and most efficient alternatives for generating power. However, the large initial capital costs of fuel cell technology have offset the advantages it offers and slowed down its adoption for widespread applications [177]. The PEMFC using hydrogen is one of the emerging fuel cells with many advantages ranging from emission of water as waste, operation at low temperatures for quick start-up, and the use of solid polymers as electrolytes, reducing both construction and safety complications [71]. This fuel cell type is seriously being considered as an alternative power source for stationary and mobile applications, but there are several technical challenges which have to be overcome before it can be adopted for use in these devices.

One of the means of reducing the cost of a PEMFC is by improving its performance through system optimisation. This facilitates the understanding of how different parameters affect the performance of the fuel cell in real operating conditions and subsequently reduce the cost involved in prototype development. Fuel cell modelling has received tremendous attention in the last two decades with the ultimate aim of better understanding the underlying phenomenon of operating fuel cells. Much research has been carried out on PEMFCs ranging from one-dimensional models, showing phenomena where mass transport limitation is taken into account, and two- or three-dimensional models encompassing thermal and water management. This two-

or three-dimensional model also combines electrochemical, thermodynamic and fluid dynamic equations. Heat transfer equations and mass and energy balances were also incorporated into some studies to provide detailed understanding of emerging processes in fuel cell systems.

In the landmark works on PEMFC by Bernardi [157], Bernardi and Verbrugge [23] and Springer *et al.* [24], which are based on one-dimensional models, the focus is on humidification requirements of inlet gases and issues related to variable membrane humidification. The work by this group [23, 24, 157] provided the required framework for the multidimensional models that followed in subsequent years. A vast number of previous works are also CFD-based. More recent works that are CFD-based can be found in [30, 53, 66, 80, 141, 178, 179]. Available experimental work to date has been conducted mostly to validate highly sophisticated CFD simulations against the cell global polarisation curves. Some of the experimental studies can be found in [68, 180-182].

Another issue of significant importance in PEM fuel cells is the pressure drop, especially at the cathode side of the cell. The product water generated at the cathode channel must be removed from the cell and this requires a high pressure drop. Too high pressure drops create excessive parasitic power requirement for the pumping of air through cells, hence, the effective design of the fuel channel is required to ensure a balance in pressure drop requirements at the fuel cell cathode section.

Inoue *et al.* [58] studied gas flow through the GDL and the internal phenomena of a single PEMFC. The result shows an increase in flow when the differential pressure between adjoining channels is increased, and an increase in the output density as the depth of the separator channel become smaller. Liu *et al.* [183] studied the two-phase flow and water flooding of reactants in the cathode flow channels of an operating transparent PEMFC experimentally. The effect of the flow field type, cell temperature, cathode flow rate and operation time on the water build-up and cell performance formed part of this study. The results indicate the adverse effect of liquid

water accumulation on mass transport and the subsequent reduction of the performance of the fuel cell.

Rodatz *et al.* [184] conducted studies on the operational aspects of a PEMFC stack under practical conditions. Their study focused particularly on the pressure drop, two-phase flow and effect of bends. They observed a decrease in the pressure drop at a reduced stack current. Maharudrayya *et al.* [185] studied the pressure drop and flow distribution in the multiple parallel channel configurations that are used in PEMFC stacks. Through their study, they developed an algorithm to calculate the flow distribution and pressure drop in multiple U- and Z-type flow configurations of a fuel cell. Ahmed *et al.* [59] used a numerical model to investigate the performance of a PEMFC at high operating current densities for various channel cross-sectional configurations, while maintaining the same reactant flow rates and inlet boundary conditions. The obtained results reveal that rectangular channel cross-sections give higher cell voltages, while the trapezoidal channel cross-section gives more uniform distributions at the membrane-cathode GDL interface. The results further reveal the presence of an optimum channel-shoulder ratio for optimal fuel cell performance.

Most of the existing models in the literature address the effect of fuel channel geometric parameters on the performance of the PEM fuel cell without investigating the mutual interdependence of the GDL porous medium, reactant gas flow rate and gas channel geometry on the fuel cell system performance. Studies on PEM fuel cell performances which incorporate the determination of optimal operating values for fuel cell design parameters, taking into consideration the combined mutual effect of channel geometry, flow rate and GDL characteristics are still very limited in the literature. A good understanding of the interactive interdependence of these fuel cell parameters is therefore essential for optimum fuel cell design. One crucial design consideration in fuel cell design is the reactant flow in the flow field because of the dominant effect of the parasitic losses caused by frictional losses, reactant consumption, species production and blockages resulting from the two-phase flow.

Therefore, the purpose of this chapter in the thesis is to investigate the effect of a range of operating conditions such as reactant flow rates, GDL porosity, channel geometry and flow orientation on the performance of a single PEM fuel cell, and also to determine the optimal operating conditions for this class of fuel cell. In addition, this chapter sought to determine the optimal fuel cell performance at different geometric configurations for a given GDL porosity and reactant species flow rate, which has not been given much attention in the literature. In this chapter, a three-dimensional steady-state computational model for a single PEM fuel cell was developed to predict the fuel cell performance under different operating conditions, and subsequently add to the knowledge base needed to produce generic design information for fuel cell systems, which can be applied to better designs of fuel cell stacks.

4.2 MODEL DESCRIPTION

Figure 4.1 shows a schematic diagram of a typical PEM fuel cell cross-section indicating the different zones and species transport across the zones. This consists of seven different regions: the cathode flow channel, cathode diffusion layer, cathode catalyst layer, PEM, anode catalyst layer, anode diffusion layer and the anode flow channel. It was assumed that the fuel used is hydrogen at the anode side which diffuses through the porous GDL and comes into contact with the catalyst layer. At this layer, it forms hydrogen ions and electrons. The hydrogen ion diffuses through the polymer electrolyte membrane at the centre, while the electrons flow through the GDL to the current collectors and into the attached electric load.

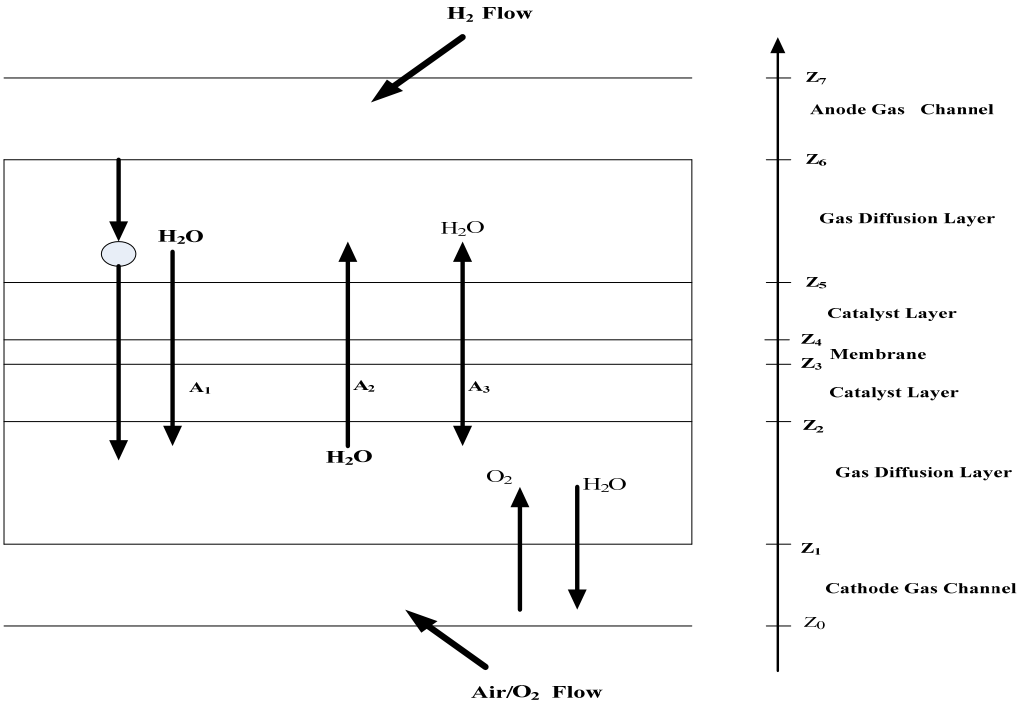

Figure 4.1 Schematic diagram of a PEM fuel cell showing different zones and species transport across the zones. The net water flux is the sum of: (A_1) electro-osmotic effect, (A_2) diffusion effect and (A_3) the permeability effect

The electrochemical reactions are:

anodic: $H_2 \rightarrow 2H^+ + 2e^-$, (4.1)

cathodic: $\frac{1}{2}O_2 + 2H^+ + 2e^- \rightarrow H_2O$, (4.2)

net reaction: $H_2 + \frac{1}{2}O_2 \rightarrow H_2O$. (4.3)

Figure 4.2 depicts the computational domain consisting of the anode flow channel, anode diffusion layer, MEA, cathode diffusion layer, and cathode flow channel. In this model, the numerical domain is a full single-cell geometry domain. Pure hydrogen and air were used as reactant gases in the model. The inlet flow velocity was controlled by the stoichiometry numbers of 1.2 at the anode and 2.0 at the

cathode. The operating pressure was 101 kPa absolute at the exit of the cell. The details of the flow field and other physicochemical parameters used for the base case are summarised in Table 4.1 and Table 4.2.

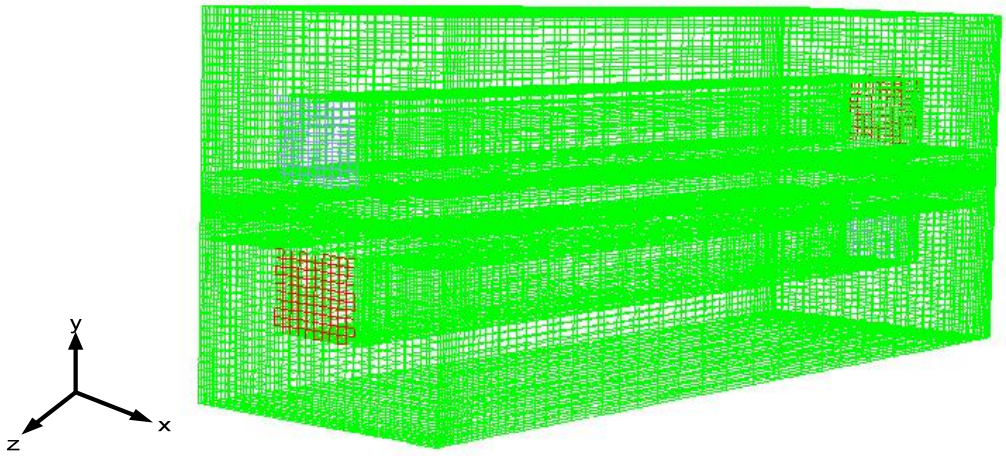

Figure 4.2 The discretised three-dimensional computational domain of a single PEM fuel cell

Table 4.1 Base case geometric parameters of the modelled fuel cell

Channel length (mm)	120
Channel width (mm)	1.0
Channel depth (mm)	1.2
Membrane thickness (mm)	0.036
Catalyst layer thickness (mm)	0.012
Electrode thickness (mm)	0.21

Table 4.2 Physicochemical properties of the modelled fuel cell

Description	Value
Cell operating temperature (^{o}C)	70
Air-side/fuel-side inlet pressure (atm)	3/3

Open-circuit voltage (V)	0.95
Porosity of GDL	0.4
Permeability of GDL (m^2)	1.76×10^{-11}
Tortuosity of GDL	1.5
Porosity of catalyst layer	0.4
Permeability of catalyst layer (m^2)	1.76×10^{-11}
Tortuosity of catalyst layer	1.5
Porosity of membrane	0.28
Permeability of membrane (m^2)	1.8×10^{-18}
Reference diffusivity of H_2	11×10^{-5} m^2 s^{-1}
Reference diffusivity of O_2	3.2×10^{-5} m^2 s^{-1}
Electric conductivity of catalyst layer $(\Omega^{-1} m^{-1})$	190
Electric conductivity of GDL $(\Omega^{-1} m^{-1})$	300
Electric conductivity in carbon plate $(\Omega^{-1} m^{-1})$	4000
O_2 stoichiometry ratio	1.2
H_2 stoichiometry ratio	2.0
Oxygen mole fraction	0.406
Relative humidity of inlet fuel/air	100%
Reference current density of anode (A/m^2)	7500
Reference current density of cathode (A/m^2)	20
Anode transfer coefficient	2.0
Cathode transfer coefficient	2.0

4.2.1 MODEL ASSUMPTIONS

Regarding the modelling of the fuel cell, the following assumptions were made:

- the cell operates under steady-state conditions;
- isothermal boundary conditions were used for external walls;
- the flow in the cell is considered to be laminar;
- reactant and products are assumed to be ideal gas mixtures; and
- the electrode is assumed to be an isotropic and homogeneous porous medium.

4.2.2 GOVERNING TRANSPORT EQUATIONS

The basic transport equation (conservation of mass and momentum) applies to the transport of gas mixtures in the gas channels in the fuel cell. The corresponding governing equations are written as follows:

Continuity equation: $$\frac{\partial(\rho v_x)}{\partial x}+\frac{\partial(\rho v_y)}{\partial y}+\frac{\partial(\rho v_z)}{\partial z}=S_m \quad (4.4)$$

where S_m is the source term, owing to electrochemical reactions corresponding to the hydrogen depletion during reactions, which is applicable at both the anode and cathode GDL/MEA interface and calculated by [178]:

$$S_m = 0, \quad z_0 \le z \le z_2 \quad \text{and} \quad (4.5)$$

$$S_m = -\frac{\lambda[H_2]}{\kappa+[H_2]}, \quad z_2 \le z \le z_3 \ , \quad (4.6)$$

where $[H_2]$ is the concentration of hydrogen in the domain of interest, and λ and κ are terms of which the values are dependent upon the rate constants for the atomic oxidation of H_2 and the platinum loading in the catalyst layer. The value of κ was set

equal to 1 and λ assumed different values, which were subject to different values of the concentration of Pt initially in the catalyst layer, as discussed by Hontanon *et al*. [178]. The momentum conservation, also referred to as the Navier-Stokes equation, is:

Momentum (*x*-direction):

$$v_x \frac{\partial(\rho v_x)}{\partial x} + v_y \frac{\partial(\rho v_x)}{\partial y} + v_z \frac{\partial(\rho v_x)}{\partial z}$$

$$= -\frac{\partial P}{\partial x} + \frac{\partial}{\partial x}\left(\mu \frac{\partial v_x}{\partial x}\right) + \frac{\partial}{\partial y}\left(\mu \frac{\partial v_x}{\partial y}\right) + \frac{\partial}{\partial z}\left(\mu \frac{\partial v_x}{\partial z}\right) + S_{px} \quad , \tag{4.7}$$

Momentum (*y*-direction):

$$v_x \frac{\partial(\rho v_y)}{\partial x} + v_y \frac{\partial(\rho v_y)}{\partial y} + v_z \frac{\partial(\rho v_y)}{\partial z}$$

$$= -\frac{\partial P}{\partial y} + \frac{\partial}{\partial x}\left(\mu \frac{\partial v_y}{\partial x}\right) + \frac{\partial}{\partial y}\left(\mu \frac{\partial v_y}{\partial y}\right) + \frac{\partial}{\partial z}\left(\mu \frac{\partial v_y}{\partial z}\right) + S_{py} \quad \text{and} \tag{4.8}$$

Momentum (*z*-direction):

$$v_x \frac{\partial(\rho v_z)}{\partial x} + v_y \frac{\partial(\rho v_z)}{\partial y} + v_z \frac{\partial(\rho v_z)}{\partial z}$$

$$= -\frac{\partial P}{\partial z} + \frac{\partial}{\partial x}\left(\mu \frac{\partial v_z}{\partial x}\right) + \frac{\partial}{\partial y}\left(\mu \frac{\partial v_z}{\partial y}\right) + \frac{\partial}{\partial z}\left(\mu \frac{\partial v_z}{\partial z}\right) + S_{pz} \quad . \tag{4.9}$$

The source terms account for situations where a fluid passes through a porous medium. The term is applicable to the electrode and catalyst zones. For low velocities encountered in fuel cells, these source terms are applicable at the GDLs and are given by Darcy's law:

$$S_{px} = -\frac{\mu v_x}{\beta_x}, \tag{4.10}$$

$$S_{py} = -\frac{\mu v_y}{\beta_y} \quad \text{and} \tag{4.11}$$

$$S_{pz} = -\frac{\mu v_z}{\beta_z} \quad \text{at} \quad z_1 \le z \le z_6 \ , \tag{4.12}$$

where μ is the fluid viscosity in the medium and β is the permeability of the electrode material. The permeability of the medium was assumed to be isotropic as stated in the assumptions in this model, hence β_x, β_y and β_z all have the same value stated in Table 4.2 (1.76 x 10^{-11} m^2). Other source terms for the equations above used in the model were taken from Dutta *et al.* [141]. The local current density, i_o, is a measure of the electrochemical reaction rate and generally given by the Butler-Volmer equation [60]:

$$i_o = i_{o,ref}\left\{\exp\left[\frac{\alpha_{an} nF}{RT}\eta\right] - \exp\left[\frac{-\alpha_{cat} nF}{RT}\eta\right]\right\} \quad , \tag{4.13}$$

where η is the overpotential and defined as

$$\eta = \left(\Phi_s - \Phi_e\right) - E_{ocv} \quad . \tag{4.14}$$

The energy conservation equation is:

$$\frac{\partial(\rho v_x h)}{\partial x} + \frac{\partial(\rho v_y h)}{\partial y} + \frac{\partial(\rho v_z h)}{\partial z} = \frac{\partial}{\partial x}\left(k\frac{\partial T}{\partial x}\right) + \frac{\partial}{\partial y}\left(k\frac{\partial T}{\partial y}\right) + \frac{\partial}{\partial z}\left(k\frac{\partial T}{\partial z}\right) + S_T \cdot \tag{4.15}$$

For the energy equation, additional volumetric sources are present, because not all chemical energy released in the electrochemical reaction can be converted to

electrical work due to irreversibilities of the process. The total source that goes to the thermal energy equation (i.e., enthalpy) is [163]:

$$S_h = h_{react} - R_{an,cat}\eta_{an,cat} + I^2 R_{ohm} + h_L \ . \tag{4.16}$$

PEMFCs operate under relatively low temperature (< 100°C) and thus water vapour may condense to liquid water, especially at high current densities. The existence of the liquid water keeps the membrane hydrated, but it also blocks the GDL passage, reduces the diffusion rate and the effective reacting surface area. The water formation and transport of liquid water is modelled by using a saturation model based on [186, 187]. In this approach, the liquid water formation and transport is governed by the conservation equation for the volume fraction of liquid water, *s*, or the water saturation [163]:

$$\frac{\partial(\varepsilon\rho_l s)}{\partial t} + \nabla\cdot\left(\rho_l \vec{V}_l s\right) = r_w \ , \tag{4.17}$$

where the subscript l represents liquid water, and r_w is the condensation rate modelled as:

$$r_w = c_r \max\left(\left[(1-s)\frac{\rho_{wv}-\rho_{sat}}{RT}M_{w,H_2O}\right],[-s\rho_l]\right), \tag{4.18}$$

where r_w is added to the water vapor equation as well as the pressure correction (mass source). The condensation rate constant is hardwired to $c_r = 100s^{-1}$. It was assumed that the liquid velocity, V_l, is equivalent to the gas velocity inside the gas channel. Inside the highly-resistant porous zones, the use of the capillary diffusion term allows the replacement of the convective term in Eq. (4.17):

$$\frac{\partial(\varepsilon\rho_l s)}{\partial t} + \nabla\cdot\left[\rho_l \frac{Ks^3}{\mu_l}\frac{dp_c}{ds}\nabla s\right] = r_w \ . \tag{4.19}$$

Depending on the wetting phase, the capillary pressure is computed as a function of s (the Leverett function) [163, 81]:

$$p_c = \begin{cases} \frac{\sigma \cos \theta_c}{(\frac{K}{\varepsilon})^{0.5}}(1.417\ (1-s) - 2.12\ (1-s)^2 + 1.263\ (1-s)^3, \theta_c < 90\ ^oC \\ \frac{\sigma \cos \theta_c}{(\frac{K}{\varepsilon})^{0.5}}(1.417\ s - 2.12\ s^2 + 1.263\ s^3), \theta > 90\ ^oC \end{cases} \quad (4.20)$$

Eq. (4.17) models various physical processes such as condensation, vaporisation, capillary diffusion and surface tension. The clogging of the porous media and the flooding of the reaction surface are modelled by multiplying the porosity and the active surface area by (1- s), respectively.

4.2.3 CHANNEL CROSS-SECTION

Flow channels in fuel cells are typically rectangular in cross-section, though other configurations such as triangular, trapezoidal, and semi-circular shapes have been explored for fuel cell designs [178]. The manufacturing processes of the flow channels in fuel cells are quite time-consuming and expensive since graphite, which is hard and brittle, is typically used as the material of choice. Hence, the making of the flow channel is a major cost in the development of a complete PEM fuel cell. In the design of small fuel cells, where the pressure drop is in the order of 0.5-1 bar [188], serpentine or interdigitated channels could be applicable, but in larger fuel cells this is not possible, as the pressure drop would be in the order of a few bars. From cost considerations and manufacturing and performance requirements, the geometrical shape of the channel cross-section has traditionally been either rectangular or square. The rectangular cross-section was used in the design of the PEM fuel cell in this study and is schematically shown in Figure 4.3.

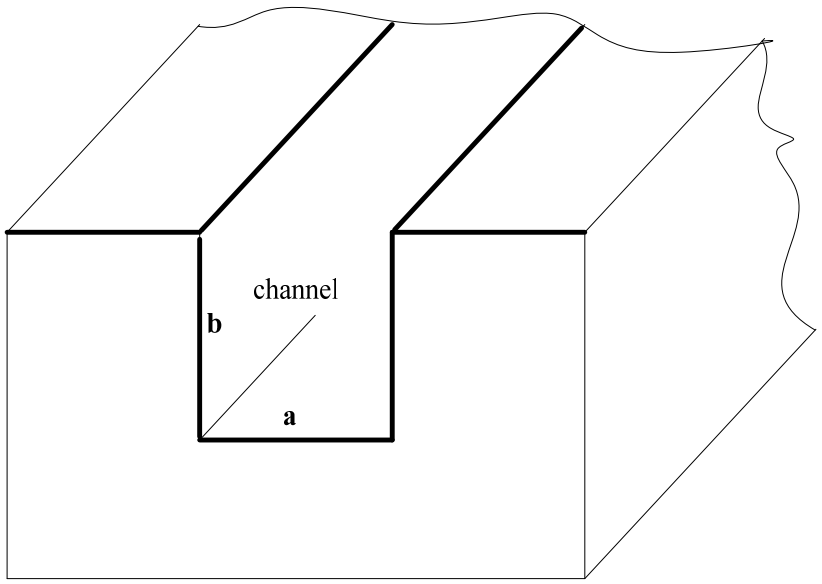

Figure 4.3 Channel cross-sectional view

For internal flows such as the ones in fuel cell channels, the Reynolds number is conventionally defined as [189]:

$$Re_{D_h} = \frac{\rho V_{avg} D_h}{\mu} \quad \text{where} \tag{4.21}$$

$$V_{avg} = \frac{\dot{m}}{\rho A_c} \; . \tag{4.22}$$

For a rectangular channel in this study, D_h is defined as [189]:

$$D_h = \frac{4A_c}{P} \; . \tag{4.23}$$

For the channel under consideration in Figure 4.3, the cross-sectional area is equal to the product of the channel width and the channel depth:

$$A_c = ab \tag{4.24}$$

and the wetted perimeter is:

$$P^* = 2(a + b) \ . \tag{4.25}$$

The pressure drop for a flow in a channel of length, *L,* is usually expressed by using the following relation [189]:

$$\Delta p = f \frac{L}{D_h} \frac{\rho V_{avg}^2}{2} \ , \tag{4.26}$$

where the friction factor, f, for steady fully-developed laminar flows in a channel with a square cross-section is given as:

$$f = \frac{56.91}{Re_{D_h}} \ . \tag{4.27}$$

Substituting the above relation Eq. (4.27) for Eq. (4.26), and taking into consideration Eqs. (4.21) to (4.25), the pressure drop can be obtained for flow channels with square cross-section (a = b), as:

$$\Delta P = 28.455\left(\frac{\mu \dot{m}}{\rho}\right)\left(\frac{L}{a^4}\right) \quad . \tag{4.28}$$

Thus, the flow channel length for flow channels with a square cross-section can be determined as:

$$L = \frac{\Delta p \rho a^4}{28.455 \mu \dot{m}} \quad . \tag{4.29}$$

Similarly, the flow channel length for a rectangular cross-section can be obtained by:

$$L = \frac{8\Delta p \rho (ab)^3}{C\mu \dot{m}(a+b)^2} \quad , \tag{4.30}$$

where $C = fRe D_h$ is a function of the b/a for rectangular flow channels [189].

The pressure drop in the channel can be obtained using the flow rate (q) – pressure drop ΔP relationship for a rectangular cross-section relation [190]:

$$q = \frac{4ba^3}{3\mu} \times \frac{-\Delta P}{\Delta L}\left[1 - \frac{192}{\pi^5 b}\sum_{i=1,3,5,}^{\infty} \frac{\tanh\left(i\pi b/2a\right)}{i^5}\right] . \tag{4.31}$$

4.2.4 FLUID FLOW THROUGH GAS DIFFUSION LAYER

In fuel cells, the fluid flow diffuses through the GDL for the reaction to take place on the MEA. The effective diffusivity for the gas-phase flow in porous media can be written as:

$$D_{eff} = D\frac{\varepsilon}{\tau} \quad . \tag{4.32}$$

The tortuosity (τ) is a difficult parameter to estimate except through experimentation. Hence, it is usually correlated in fuel cell studies using a Bruggeman correlation. This correlation assumes that τ is proportional to $\varepsilon^{-0.5}$, resulting in the simpler expression [191]:

$$D_{eff} = D\varepsilon^{1.5} \, . \tag{4.33}$$

The porosity correlation is used to adjust for the longer effective path length through the porous media.

4.2.5 BOUNDARY CONDITIONS

Pressure boundary conditions were specified at the outlets since the reactant gas flow is usually separate and at different pressures. The inlets were all assigned as mass flow inlets. The GDL and the catalyst layer were surrounded by sealed plates at the inlet and outlet planes, so the boundary conditions at the inlet and outlet planes take the no-slip condition for the velocity and non-permeable condition for the species mass fraction. The membrane-electrode interface was defined as a wall, primarily to inhibit species and electron crossover through the membrane. This also prevents pressure problems at the interface. In the areas at which the gas diffusion electrodes were in contact with the bipolar plates, a constant reference voltage equal to zero was assigned as a boundary condition both at the anode and at the cathode terminals. The electron flux was set to zero at all other walls. The anode was grounded (V = 0) and the cathode terminal was set at a fixed potential (0.75 V), less than the open-circuit potential (0.95 V). Both anode and cathode terminals were assigned wall boundaries.

4.2.6 SOLUTION TECHNIQUE

The model equations were solved using the CFD software ANSYS Fluent® 12.0 with Gambit® (2.4.6) as a pre-processor. The CFD code has an add-on package for fuel cells, which has the requirements of the source terms for species transport equations, heat sources and liquid water formations [163]. Control volume technique was used for solving the problem. The meshes were more refined at the membrane-catalyst assembly regions. The conservation of mass, momentum and energy equations in the three-dimensions were solved in turn, until the iterative process met the convergence criteria. In this study, the definition of convergence criteria indicates that the largest relative error between two consecutive iterative residuals within the overall computational domains is less that 10^{-6}.

The domain was divided into hexahedral volume elements. A computational mesh of about 257 346 volume elements was obtained with the grid. The grid independence was verified at the preliminary test runs. Four structured grid configurations were evaluated for the PEMFC. The number of elements in the *x-, y-* and *z*-directions was: (a) 70 × 70 × 25, (b) 87 × 87 × 34, (c) 104 × 87 × 34 and (d) 104 × 104 × 43. The influence of the number of elements on the local current density at an operating voltage of 0.4 V was investigated. The local current density for grid (a) differs from that of (b-d) with a deviation of about 4.2%. However, the local current density distributions for grids (b), (c) and (d) do not show any significant differences. The difference between the local current densities for (b) and (c) is about 0.36% and the difference between (c) and (d) is 0.48%. Grid (c) was chosen for the simulations as a trade-off between accuracy and cost of time.

The solution strategy was based on the SIMPLE algorithm [192]. Momentum equations were solved for the velocity followed by solving the continuity equation, which updates the pressure and the flow rate. Results were then verified for convergence. The simulation for each operating potential converged in 45-60 minutes

depending on the current density on an Intel® Core(TM) 2Duo 3.00 GHz PC with 3.24 GB of DDRam.

4.2.7 MODEL VALIDATION

The validation of physical and numerical models is very important, hence comparison with available experimental data is highly desirable. To describe the performance of fuel cells, polarisation curve or voltage-current curve is often used. Also, by comparing the polirisation curve from modelling with experiments, the accuracy or otherwise of a model could be validated [193]. The polarisation curve obtained for the base case operating conditions have been compared with experimental measurements of Wang *et al.* [33] and Cheng *et al.* [60] and are shown in Figure 4.4. There is a good agreement between the experimental curves in the low load region. However, the model current density in the high mass transport limited region (> 2.75 A/cm^2) is higher than the experimental values.

This observation is common in models where the effect of reduced oxygen transport, due to water flooding at the cathode at higher current density, cannot be properly accounted for [99]. Nonetheless, the prediction from the model could still be used successfully for better understanding of the complex processes in fuel cell systems.

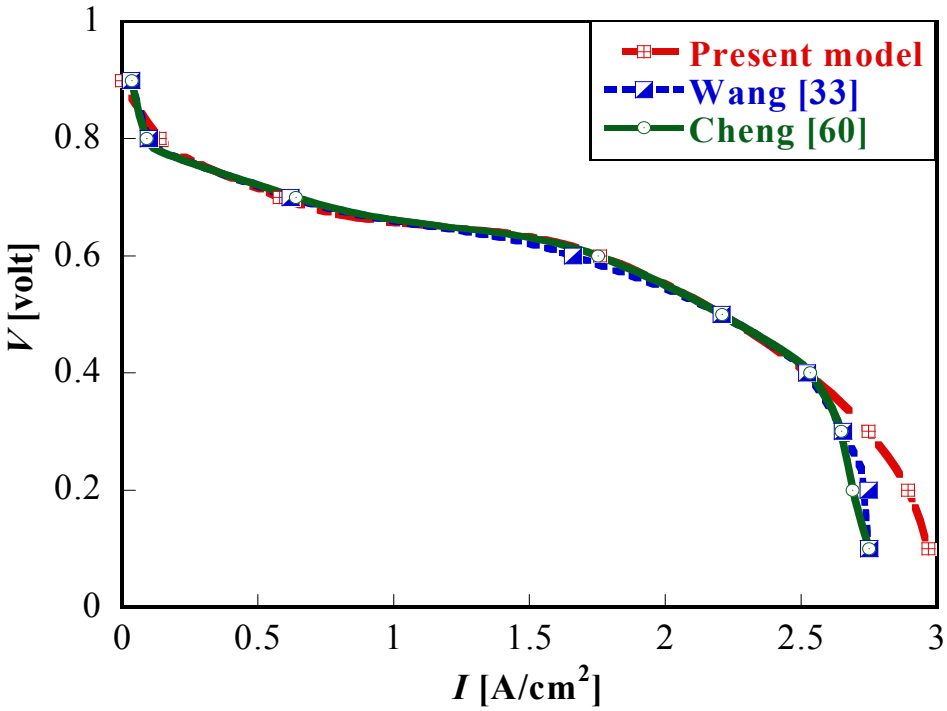

Figure 4.4 Comparison of numerical model prediction and experimental polarisation curves at base condition

4.3 MODEL RESULTS AND DISCUSSION

4.3.1 PRESSURE DROP IN FLOW CHANNEL

Figure 4.5 shows the calculated pressure drops for the rectangular flow channel over a range of air mass flow rates at a channel depth and width of 1.2 mm and 1.0 mm, respectively. The results indicate that the pressure drop increases as the mass flow rate at the cathode is increased. This is expected since an increase in the mass flow rate increases the reaction of the reactant species and also reduces the resident water in the cathode channel of the fuel cell. Generally, fuel cells with high pressure drops in the flow field exhibit a more even distribution of the reactant species flow than those with low pressure drops in their flow fields. These even distributions of reactant species greatly enhance the fuel cell performance [194].

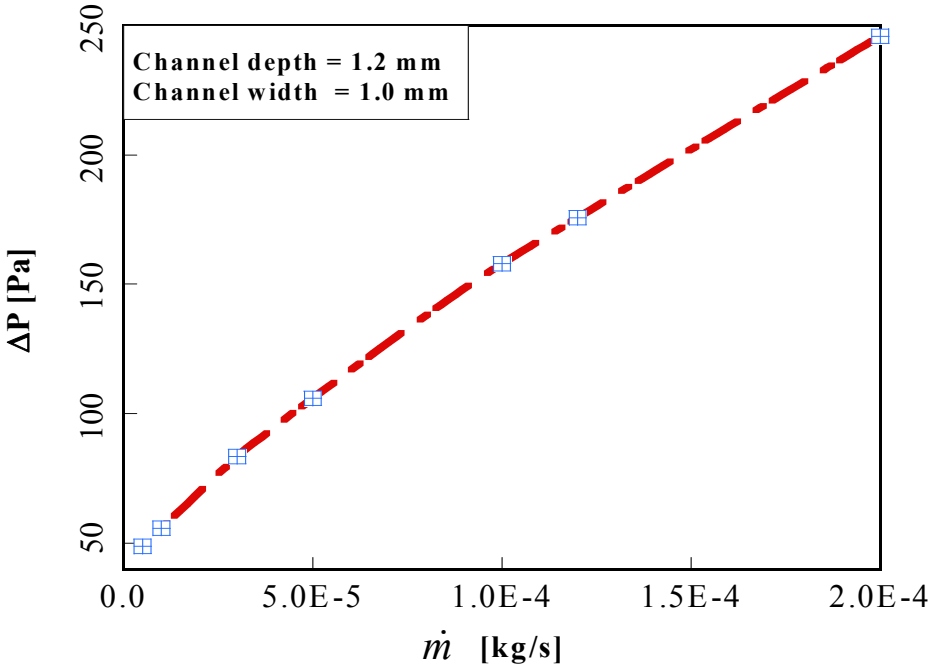

Figure 4.5 Pressure drop along the model flow channel at base operating conditions for a channel depth of 2.0 mm and width of 1.2 mm

4.3.2 EFFECT OF PHYSICAL PARAMETERS ON PROTON EXCHANGE MEMBRANE FUEL CELL PERFORMANCE

Figure 4.6 illustrates the polarisation curves obtained from the model (cell voltage 0.3 V) at several operating temperatures from 60-90^{o}C at stoichiometry ratios of 1.2 and 2.0, respectively, for the anode and the cathode. The curve indicates that the fuel cell performance increases with an increase in temperature and is at the optimum at temperatures of approximately 60-80^{o}C. This is consistent with literature [179, 195]. The increase in fuel cell performance with the increase in temperature can be attributed to an increase in gas diffusivity and membrane conductivity at higher operating temperatures.

The polarisation curves are also lower at 75-80 ^{o}C compared with 60-70 ^{o}C in the lower current density region, primarily due to the lower reaction rates resulting in low water content in the membrane. The condensation of water easily occurs at lower

temperatures resulting in the flooding and deterioration of the gas diffusivity in the catalyst layer and the GDLs. At temperatures beyond 80°C, the cell performance declines, since membrane conductivity decreases at high temperatures due to the onset of reduction in relative humidity of reactant gases and water content in the membrane.

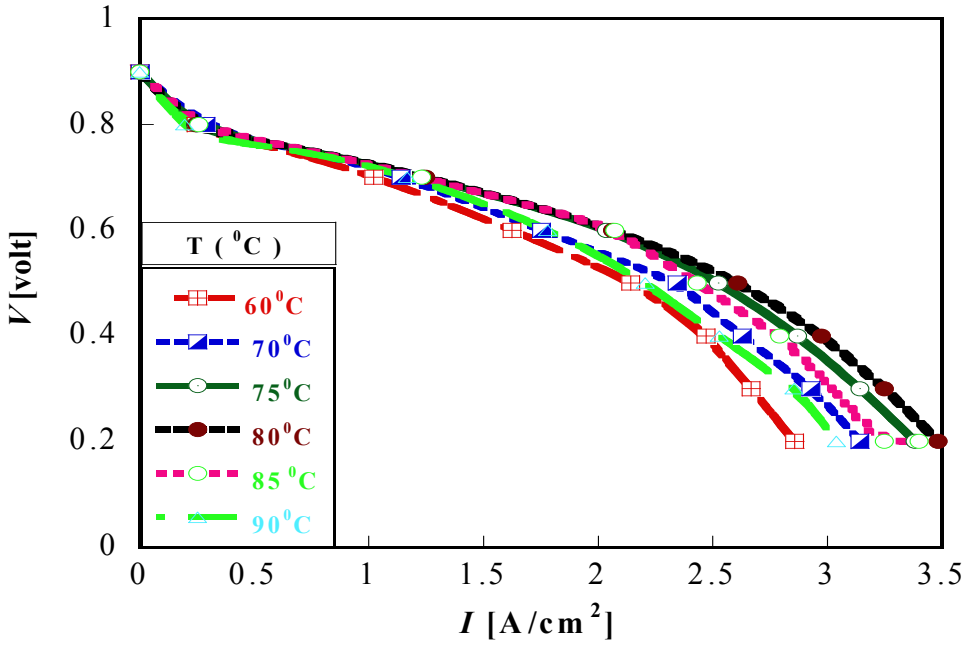

Figure 4.6 Effect of temperature on cell performance at base conditions

Hence, the fuel cell performance is adversely affected at temperatures between 80 and 90°C. Increasing the cell temperature beyond 80°C, results in higher levels of water loss in the cell until a critical temperature is attained where the evaporated water is greater than the amount of water being generated in the cell, thereby resulting in a total dry-out of the membrane. This could eventually lead to fuel cell failure. This model ascertains the fact that these fuel cells need to be operated at temperatures below 80°C. A humidifier may be required if operation at higher temperatures is required but this adds to the capital and running costs of fuel cells.

Figure 4.7 shows the effect of changing the oxygen mass flow rate from 5.0E-06 to 1.6E-04 kg/s on the fuel cell performance. When the cathode gas mass flow rate is increased, the fuel cell performance is enhanced, especially at lower operating fuel

cell voltages. The reason is the increase in oxygen gas through the GDL to the reaction sites, which increases the rate of reaction. At low operating voltages, more liquid water is produced, due to stronger electrochemical reaction rates, which is expected to reduce fuel cell performance.

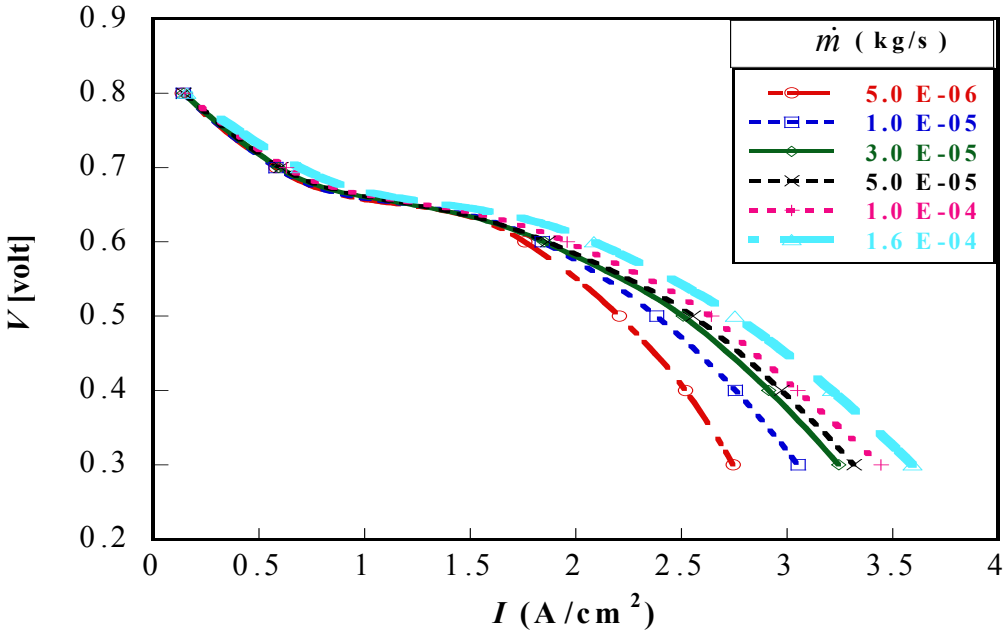

Figure 4.7 Effect of cathode gas flow rate on cell performance at base conditions

However, the high oxygen mass flow rates in the porous layer generate high shear forces, which aid the transport of liquid water downstream in the flow channel along the flow direction. The effect is minimal at high operating voltages as observed on the curves, primarily due to low membrane humidification. Wang and Liu [196] obtained similar results in their experimental work on PEM fuel cell performance. This is because a low amount of water presence occurs at these voltage levels, due to slow reaction rates coupled with an increase in the oxygen gas supply which results in reduced cell performance.

The effect of the GDL porosity on the performance of the PEM fuel cell is shown in Figure 4.8. The results show the fact that the effect of the GDL porosity on fuel cell performance is significant when the GDL is in the low value region (0.1-0.4).

Increasing the diffusion layer porosity size has an increasingly weaker effect on the performance. A GDL porosity beyond 0.6 does not have a significant effect on the fuel cell polarisation curve. This observation is in agreement with the optimisation work of Lin *et al.* [195]. They reported an optimum GDL porosity of 0.5913 for the PEM fuel cell modelled in their study. Therefore, maintaining a porosity level between 0.4 and 0.6 is a reasonable value for the fuel cell if durability issues in the fuel cell structure are taken into consideration.

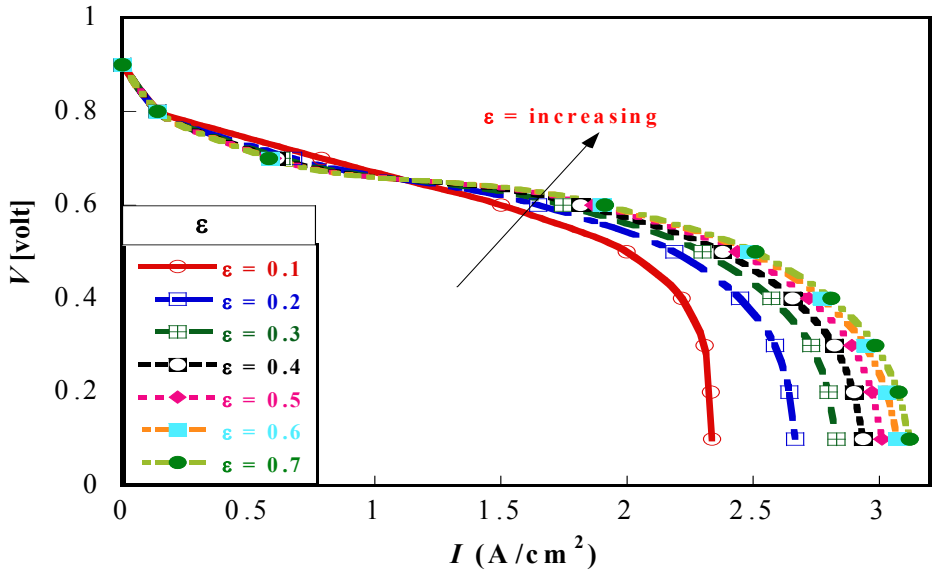

Figure 4.8 Effect of gas diffusion layer porosity on cell performance at base conditions

Fuel cell performance is also largely influenced by the operating pressure. In this study, the fuel cell operating pressure varied from 1-5 atm at a constant operating temperature of 70^{o}C. The polarisation curves for different operating pressures are shown in Figure 4.9. As the operating pressure increased from 1-5 atm, the fuel cell performance also improved. There was a significant increase in the fuel cell performance from 1-3 atm, however, after 3 atm the increase was minimal. Increasing pressure improves the reactant's interaction with the electrolyte, hence increasing fuel cell performance. The pressure impact on the fuel cell performance is prominent at a higher current density of operation. Generally, the polarisation curve shifts position positively as the pressure increases.

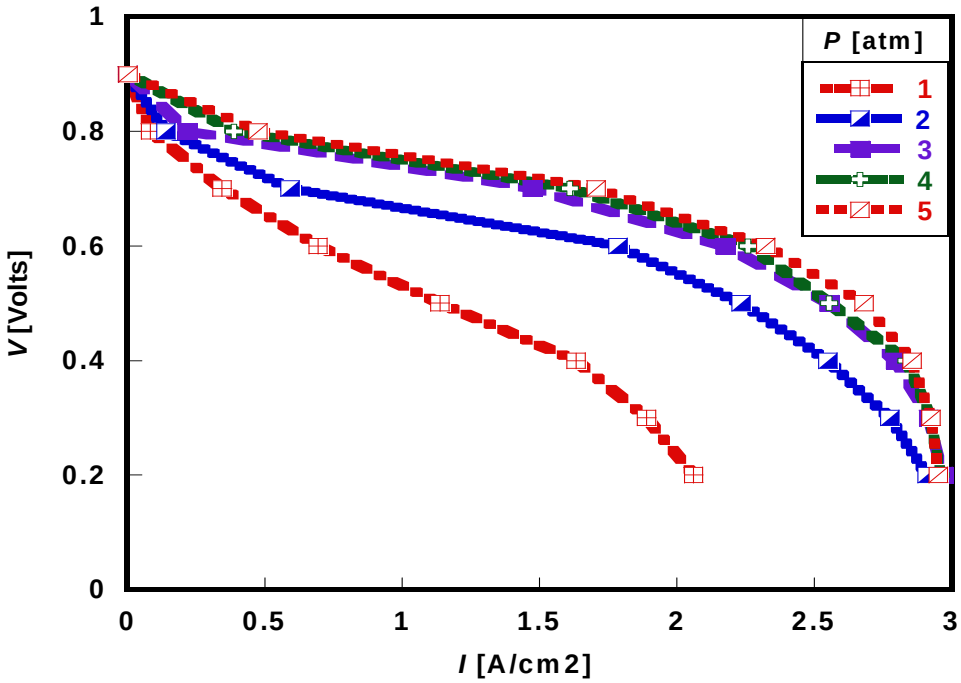

Figure 4.9 Effect of operating pressure on cell performance at base conditions

Figure 4.10 shows the effect of changing the cathode gas stoichiometry ratio on the fuel cell performance. The temperature, pressure and porosity were maintained at constant values of 70^{o}C, 2 atm and 0.4, respectively. Very small changes in the overall cell performance are observed at an increased cathode gas stoichiometry, especially at higher operating current densities. Performance at low stoichiometries

(<3.0) shows a reduced fuel cell performance and at higher levels (>3.5) the increment becomes insignificant. This increase in performance is due to the increment in oxygen availability and the humidity of the membrane. At low cathode gas stoichiometry, there are limitations of oxygen availability towards the end of the flow channel and, furthermore, the water removal rate is reduced leading to a reduction in performance. Operating a fuel cell at lower voltages increases electrical resistance within the cell that also hinders an increase in performance. However, performance could be augmented by increasing the stoichiometry rate at these operating voltages.

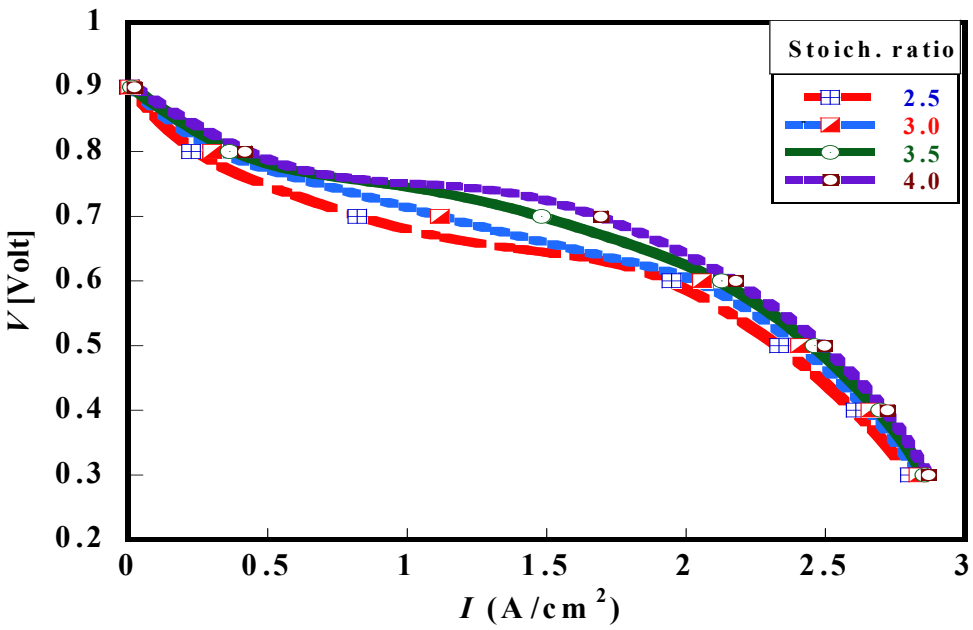

Figure 4.10 Effect of cathode gas stoichiometry on cell performance at base conditions

4.3.3 EFFECT OF DESIGN PARAMETERS ON PROTON EXCHANGE MEMBRANE FUEL CELL PERFORMANCE

Simulations were performed for different sets of channel dimensions. Two different parameters, i.e., channel width and channel depth, were chosen for the study. Figure 4.11 illustrates the effect of channel depth on the fuel cell performance at a constant channel length. The optimal current density for the fuel cell was obtained at a channel depth of 2.0 mm (current density: 2.62 A/cm^2). A further increase in depth showed a decline in fuel cell performance.

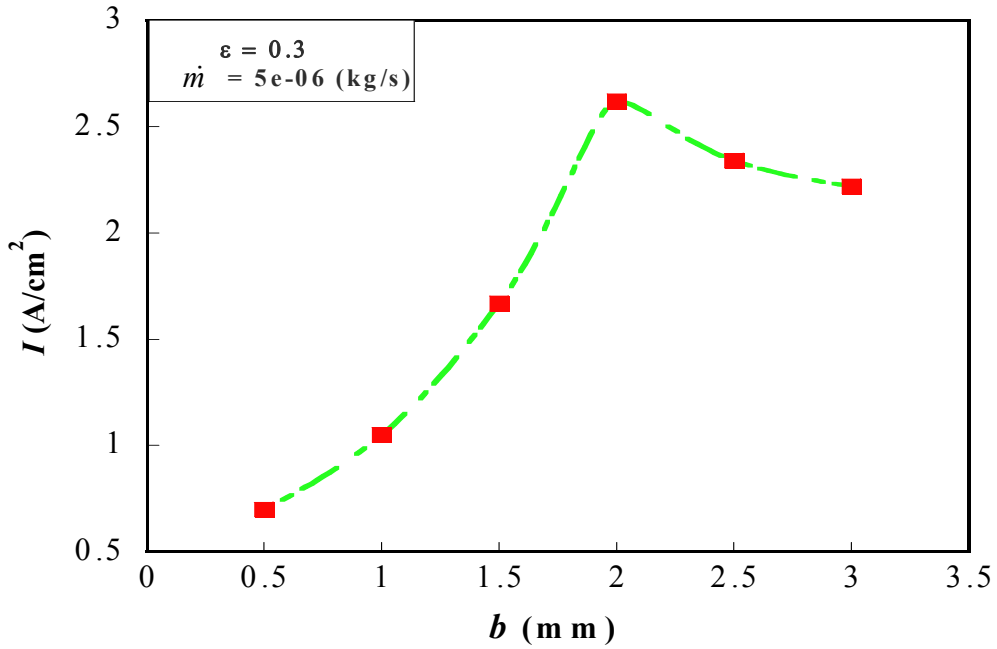

Figure 4.11 The cell current density at different channel depths at a cell potential of 0.3 V, a temperature of 70 °C and a mass flow rate of 5e-06 kg/s

Figure 4.12 shows the fuel cell performance for the six cases of channel widths considered. Performance increased gradually from case 1 (0.6 mm – current density: 1.30 A/cm^2) until an optimum was obtained at case 4 (1.2 mm – current density: 2.45 A/cm^2).

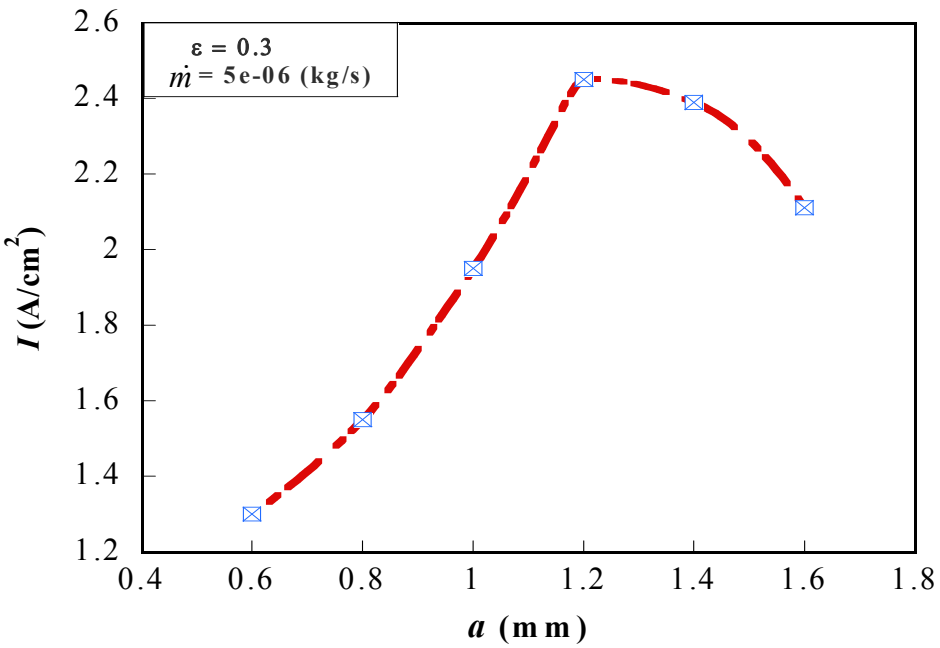

Figure 4.12 The cell current density at different channel widths at a cell potential of 0.3 V and a temperature of 70 ºC

Increasing the channel width beyond 1.2 mm showed a reduction in fuel cell performance. These results were consistent with those observed by other researchers. Watkins *et al.* [197] studied optimal dimension for cathode-side channels. They claimed that the most preferred ranges are 1.02-2.04 mm for channel depths and 1.14-1.4 mm for channel widths. Figures 4.11 and 4.12 suggest the existence of an optimal channel depth and width for the PEM fuel cell that will offer the best system performance.

The effect of species flow orientation on the performance of the fuel cell was investigated for the base case. It was found that the direction of flow affects the performance of the fuel cell. Co-flow and counterflow affect the fuel cell performance at different operating cell voltages. Figure 4.13 depicts the fuel cell performance at the base case conditions and, for a channel depth and width of 2.0 mm and 1.2 mm, respectively, the counterflow and the co-flow orientations. Current densities of 2.61 A/cm^2 and 2.54 A/cm^2 were obtained for the counterflow and co-flow cases,

respectively. Counterflow creates better performance for the fuel cell, especially at higher current voltages.

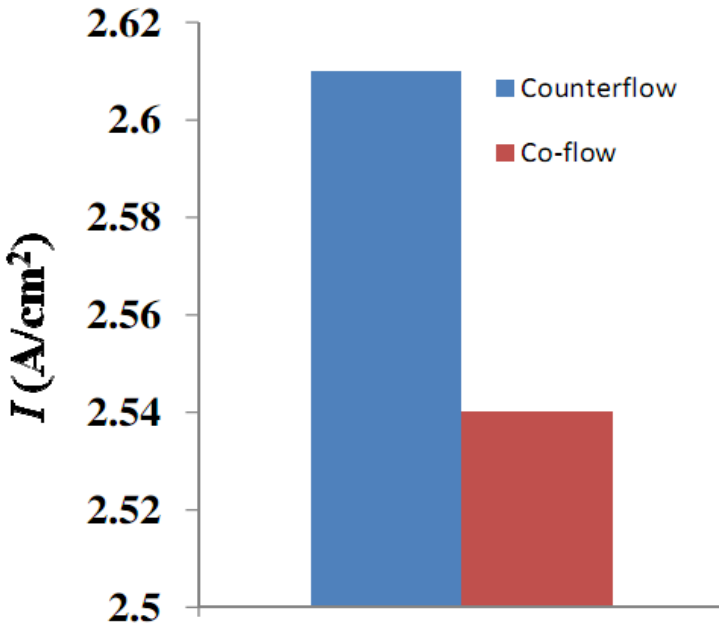

Figure 4.13 The cell current density for counterflow orientation (2.61 A/cm^2) and co-flow orientation (2.54 A/cm^2) at base case conditions, for a channel depth of 2.0 mm and a channel width of 1.2 mm

Figure 4.14 shows the contours of mass fraction for hydrogen at the anode flow channel for counterflow (Figure 4.14a) and co-flow cases (Figure 4.14b), respectively. The contour shows that counterflow configuration allows more uniform distribution of the hydrogen species at the anode flow channel, which subsequently improves the performance of the fuel cell. The effective species distribution generally aids reaction on the membrane sites and this leads to increased current density.

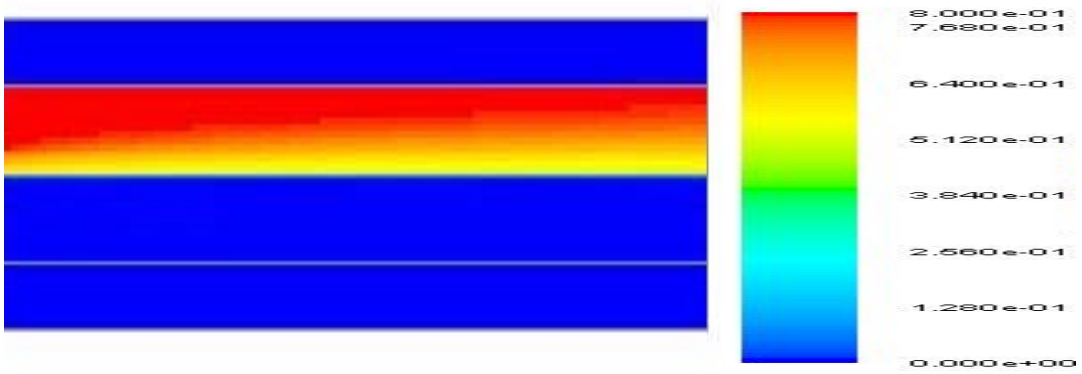

(a.) Counter flow

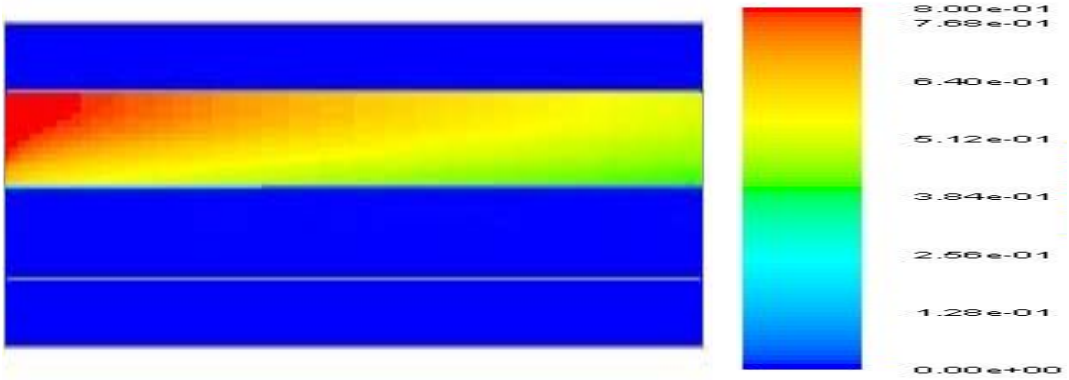

(b.) Co-flow

Figure 4.14 Contours of mass fraction of hydrogen at the anode for (a.) counterflow and (b.) co-flow cases at the base case operating conditions

4.3.4 OPTIMAL CHANNEL GEOMETRY

The results in Section 4.3.3 (Figures 4.11 and 4.12) depict the existence of an optimal channel depth and width for a PEM fuel cell system. The search for an optimal channel depth and width was carried out for the PEM fuel channel at varying GDL porosities. The first run of the simulation was carried out by fixing the cathode gas flow rate at 5e-06 kg/s, width of channel at 1.2 mm, cell operating voltage at 0.3 V and GDL porosity at 0.2. The channel depth was then varied between

0.5 and 3.0 mm. An optimal channel depth, b_{opt} , was found for this configuration. The procedure was repeated for other values of GDL porosities in the range of $0.2 \leq \varepsilon \leq 0.6$ as shown in Figure 4.15, until an optimal channel depth, which corresponds with the maximum current density, was obtained at each value of the GDL porosity.

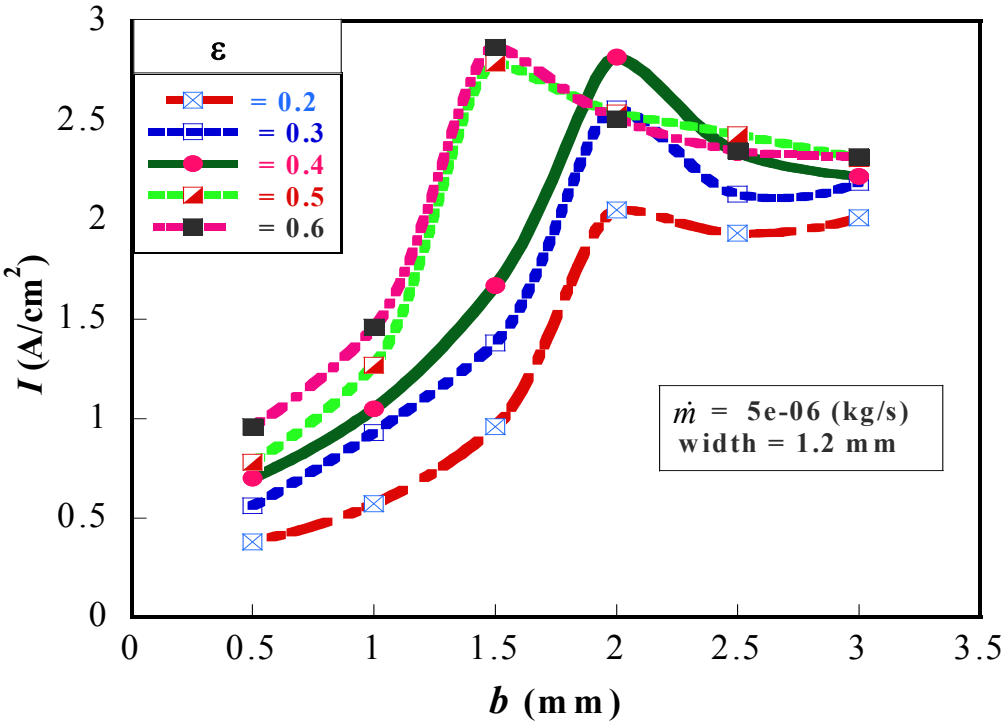

Figure 4.15 Effect of porosity and channel depth on the cell current density

Figure 4.16 gives the optimum channel depth, b_{opt}, for different cathode gas mass flow rates for different gas diffusion layer porosities. The optimal channel depth decreases as the mass flow rate increases.

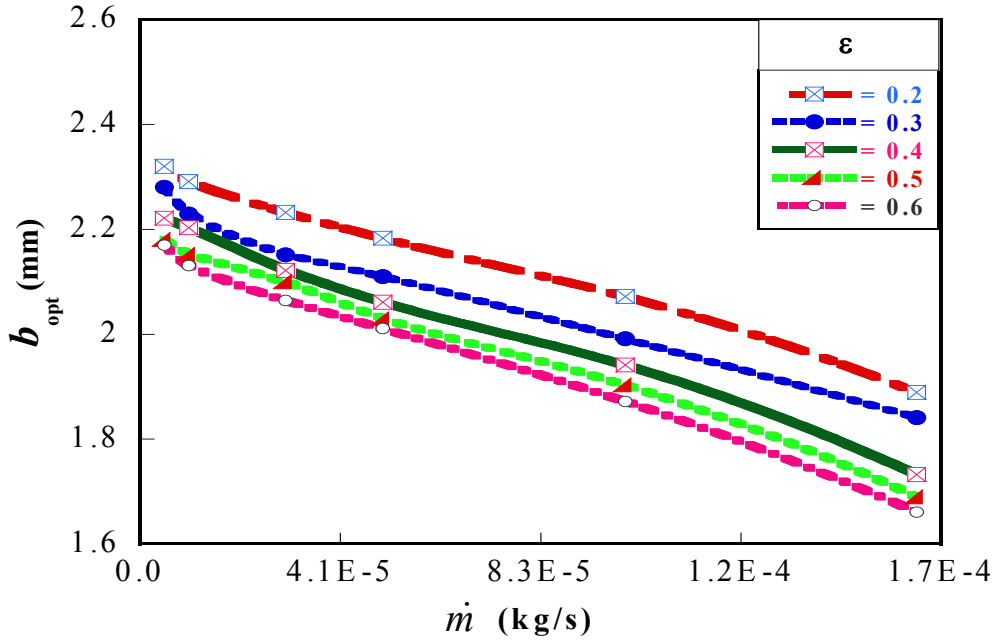

Figure 4.16 Optimum depths as a function of flow rate and gas diffusion layer porosity

Figure 4.17 shows the behaviour of the maximum current density, I_{max}, with varying cathode gas mass flow rates. Each point of the figure depicts the result of a full optimisation with respect to channel depth. The graph shows that maximised current density increases as the mass flow rate of the reactant gas increases. In each case, there is an optimal channel depth that maximises the current density of the fuel cell. Similarly, the search for optimal channel widths, a_{opt}, corresponding to the maximum current density, I_{max}, was carried out as conducted for the channel depths. Figure 4.18 shows the current density value as a function of the channel widths for different values of GDL porosities. The cathode gas mass flow rate and channel depth were initially fixed at 5e-06 kg/s and 2.0 mm, respectively.

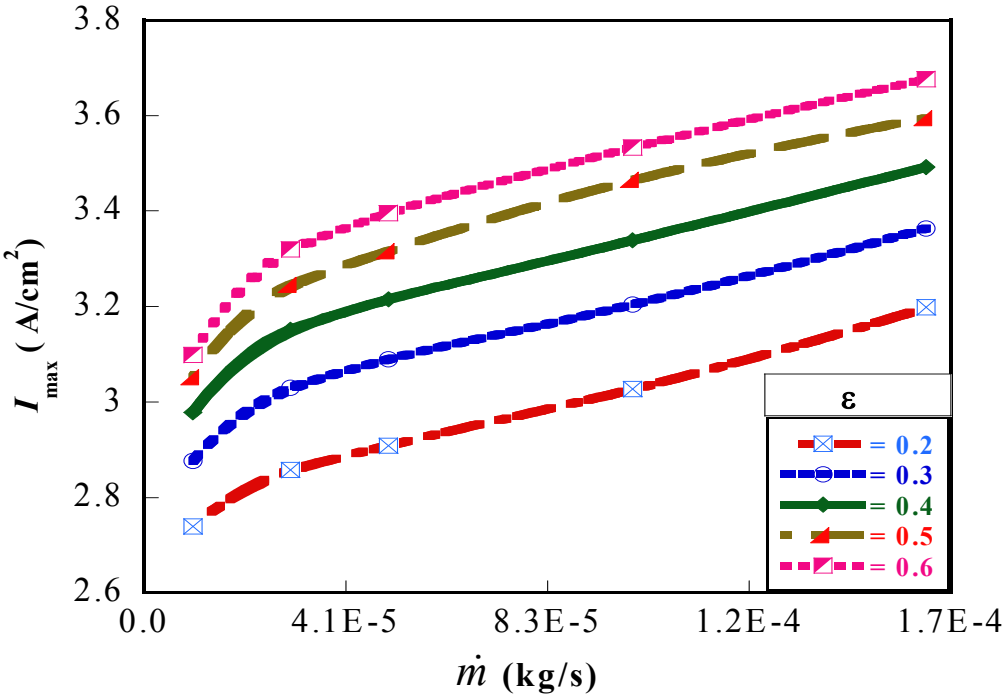

Figure 4.17 Effect of flow rate and gas diffusion layer porosity on the cell current density

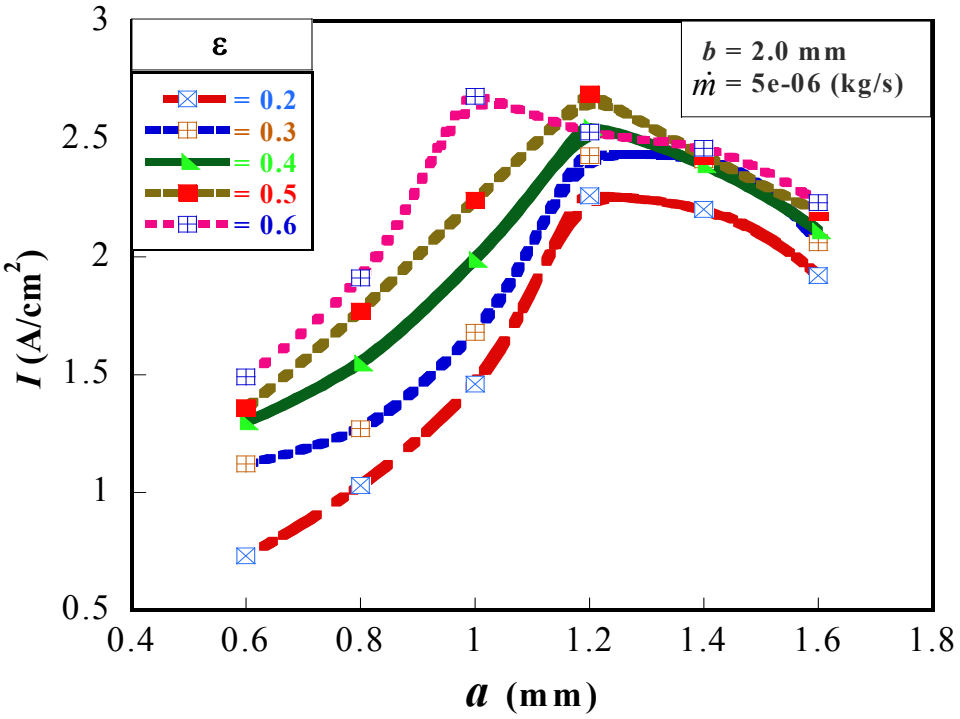

Figure 4.18 Effect of porosity and channel width on the cell current density

Figure 4.19 depicts the optimal value of the channel width as a function of the cathode gas mass flow rate for each of the values of GDL porosities ($0.2 \leq \varepsilon \leq 0.6$). The optimal channel widths, a_{opt}, from the figure decreases as the mass flow rate increases. The results obtained from Figures 4.16 and 4.19 both suggest that optimal channel depth and width decrease at increasing cathode gas mass flow rates. In designing PEM fuel cells, it can be concluded that the matching of fuel cell operating conditions and gas fuel channel configuration is very important for optimum operation issues.

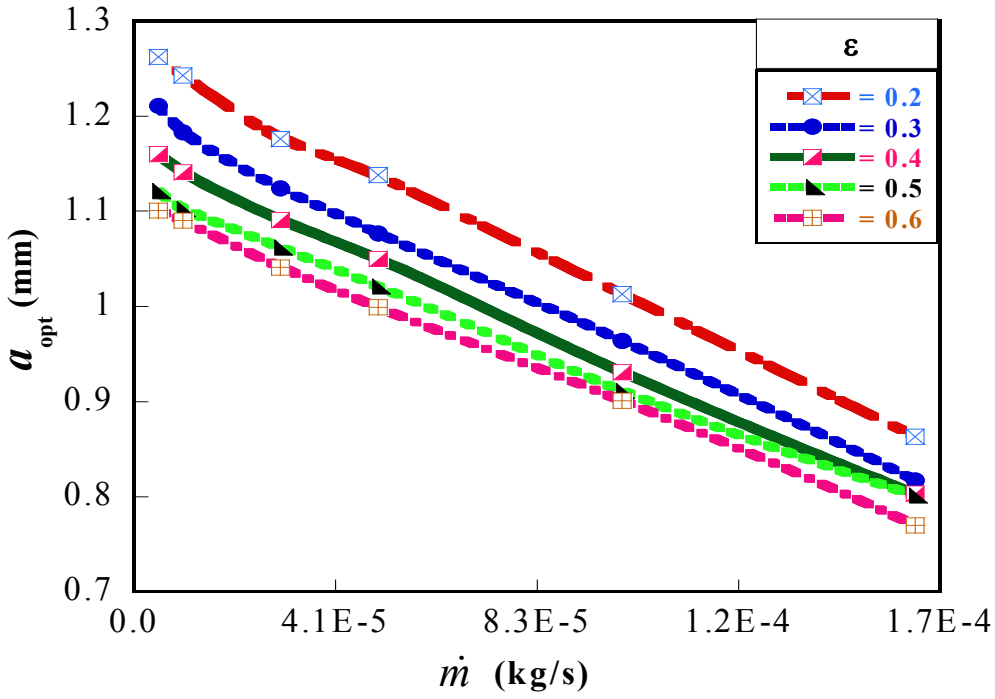

Figure 4.19 Optimum widths as a function of flow rate and gas diffusion layer porosity

CONCLUSION

In this chapter, a steady-state three-dimensional computational model was established to study the performance of a single-channel PEMFC under varying operating conditions. The model prediction was validated by its good agreement with available

experimental results. The numerical results provided detailed information on the effect of varying operating parameters of a single-channel fuel cell performance. It was proved that temperature, GDL porosity, cathode gas mass flow rate and species flow orientation affect the performance of the fuel cell. Specifically, we show that fuel cell performance increases with an increase in temperature from 60-80^{o}C. Further increases in temperature, beyond 80°C, shows a decline in fuel cell performance. The porosity of the GDL also affects the fuel cell performance. The porosity effects on fuel cell performance are more significant at porosity levels of 0.1-0.4 than at porosity levels of 0.5-0.7. The effect of the operating and design parameters on PEM fuel cell performance is also more dominant at low operating cell voltages than at higher operating fuel cell voltages. In addition, this study establishes the need to match the PEM fuel cell parameters such as porosity, species reactant mass flow rates and fuel gas channels geometry in the system design for maximum power output.

5

CHAPTER 5: OPTIMISING REACTANT GAS TRANSPORT IN A PROTON EXCHANGE MEMBRANE FUEL CELL WITH A PIN FIN INSERT IN CHANNEL FLOW

5.1 INTRODUCTION

The flow distribution in a fuel cell bipolar plate is one of the most important enhancing factors of PEM fuel cell systems. One of the critical issues in PEM fuel cell design is the efficient design of the flow channels to ensure uniform distribution of the reactant gases in the fuel cell stack. The flow field geometry and pattern have great influence on the reactant gas transport, water management and the efficient utilisation of the fuel. The flow field design of fuel cells is one of the critical technical challenges for PEM fuel cell designs and operation and impacts on the performance and the life-span of the system [65, 198].

Several studies have been carried out in recent years to improve fuel cell performance through flow-field design such as parallel, serpentine, interdigitated and many other novel combinations of these conventional types [30, 94, 69, 185, 199]. The serpentine channel type is the most widely used among the studied flow channels due to its outstanding performance when compared with others under the same operating and design conditions [197]. However, a serpentine flow field has its associated problems and is not an ideal flow field configuration. Some of the associated problems are:

- high reactant pressure loss resulting in significant parasitic power requirement to pressurise air, especially at the cathode section [62];

- loss of reactant gas concentration along the channel from the inlet towards the outlet, and membrane dehydration near the channel inlet region;
- resultant liquid water flooding near the exit region of the channel, as a result of excessive liquid water carried downstream by the reactant gas stream and collected along the flow channel [117];

These serpentine flow channel characteristics proved their effectiveness in small cells ($\leq 560 \times 250 \times 330$ mm and power rating ≤ 1000 W) where the pressure drop is in the order of 0.5-1 bar. However, serpentine flow channels perform poor for larger cells ($> 560 \times 250 \times 330$ mm and power rating ≥ 1500 W) where the pressure drop is in the order of a few bars [56]. Hence, parallel flow channels have several applications, especially for larger cell applications, but the problems of cathode gas flow distribution and cell water management need to be solved.

In these channels, apart from issues related to maldistribution of reactant gases, water coalescence forms droplets of varying numbers and sizes in the channels. This subsequently forces the reactant gas to flow preferentially through the path of least obstruction [70]. Performance improvement for this type of channel and others have been documented in the literature, but there is little information in the open literature regarding the design procedure and cross-sectional dimensions that includes pressure drops for flow in the channels [62]. Performance improvement of PEM fuel cells can be achieved in many ways and researchers have developed varieties of flow-field layouts for this purpose.

An interdigitated flow-field design was first proposed by Nguyen [200] with the addition of baffles at the end of the channels. The design forces the reactants through the GDL and the generated shear forces help blow the trapped water into the inner layer of the electrodes resulting in better fuel cell performance. Kumar and Reddy [201] presented a three-dimensional steady-state numerical mass-transfer single-cell model for a PEM fuel cell, by using metal foam in the flow field of the bipolar/end

plates rather than using conventional rectangular channels. Their result showed a significant effect of the metal foam on the permeability of the reactant species, which improved the performance of the fuel cell. They proposed the use of metal foam instead of conventional rectangular channels, especially in thinner channels where there are manufacturing constraints.

Liu *et al.* [85] investigated the effect of baffle-blocked channels on the reactant transport and cell performance using a conventional parallel flow field. Their results showed improved cell performance due to an increasing reactant spread over the GDL which enhances chemical reactions. Soong *et al.* [86] developed a novel flow channel configuration by inserting baffles in the channel of conventional flow fields to form a partially blocked fuel channel. They discovered that enhanced fuel cell performance could be achieved by reducing the gap size and/or increasing the baffle number along the channel, though with the penalty of higher pressure loss.

Liu *et al.* [87] studied the reactant gas transport and cell performance of a PEM fuel cell with a tapered flow channel design. The results obtained from the study revealed that fuel cell performance can be enhanced with a tapered fuel channel and enhancement is more prominent at lower cell voltage. The reactant gas in the tapered channel is accelerated and forced into the GDL, thereby enhancing the electrochemical reaction that improves cell performance. Xu and Zhao [61] presented a new flow-field design, termed the convection-enhanced serpentine flow field (CESFF) for polymer electrolyte-based fuel cells. They observed that the CESFF design induces larger pressure differences between adjacent flow channels over the electrode surface when compared with the conventional flow field. This design characteristic increases the mass transport rates of reactants and products to and from the catalyst layer and reduces liquid water entrapped in the porous electrode which subsequently, enhances fuel cell performance.

Wang *et al.* [78] similarly studied the use of baffles in a serpentine flow field to improve cell performance. The results showed that the novel baffle serpentine flow field, even though it induces larger pressure differences between adjacent flow channels over the entire electrode surface than the conventional serpentine design does; helps gas diffusion which leads to enhanced current density and improved cell performance.

These investigations have shown that the addition of bluff bodies (baffles) in the flow channels can increase the convection of reactants through the GDL thereby enhancing fuel cell performance. This enhanced performance and operating stability in fuel cells are achieved through improved reactant mass transport. Meanwhile, a proper understanding of the phenomenon of mass transfer through the GDL, under the influence of disturbances along the flow channels and associated pressure drop, will facilitate a proper design of PEM fuel cells.

From the literature survey above, it is clear that issues of high penalty in terms of pressure loss due to high flow resistance occur in most of the baffle-enhanced PEM flow-field designs and therefore need to be addressed. In addition, to the best knowledge of the authors, the application of pin fins for performance enhancement in PEM fuel cells has not been examined before, especially for determining the optimal geometry of the employed pin fins in PEM flow channels. Therefore, one of the major objectives of this study is to investigate the effect of a pin fin insert in the flow field of a fuel cell with the aim of improving performance as well as pressure drop along the fuel cell flow channel. The cell overpotential at the anode side of the PEM fuel cell is negligible in comparison with the cathode-side overpotential [32], hence the choice of considering oxygen mass transport at the cathode side of the fuel cell system.

Extended surfaces (fins) are frequently used in heat exchanging devices for the purpose of increasing the heat transfer between the primary surface and the

surrounding fluid. Extended surfaces of various shapes have been employed for this purpose in heat and mass transfer studies, ranging from relatively simple shapes, such as rectangular, square, cylindrical, annular, tapered or pin fins, to a combination of different geometries. Literature shows that pin fins are some of the most widely employed extended surfaces considering its hydrodynamics along flow channels [202-204]. A pin fin is a cylinder or other shaped element attached perpendicularly to a wall, with the transfer fluid passing in cross-flow over the element. Pin fins with a height to diameter ratio between 0.5 and 4 are accepted as short fins, whereas long fins have a pin height to diameter ratio exceeding 4 [203]. The effective selection of the pin fin geometric parameters will result in the improvement of the reactant gas distribution in the flow channel due to the mixing of the main flow and/or the flow in the near-wall region and, subsequently, will permit effective reactant spread over the GDL.

In the present work, the main motive is to investigate the effect of pin fins transversely arranged along the flow channel on the reactant gas distribution, and pressure drop characteristics of the fuel cell reactant gas channel. Pin fins of small hydraulic diameter, which can reduce the additional pressure drop, are employed and the effect on PEM performance is investigated. In addition, a mathematical optimisation tool is used to select the best pin fin geometric configuration that improves the fuel cell performance at a reduced pumping power requirement penalty in the PEM fuel cell flow channel. This chapter presents a novel approach at enhancing the oxygen mass transfer through the PEM fuel cell GDL at a reduced pressure drop.

5.2 MODEL DESCRIPTION

In this chapter, a two-dimensional half-cell model of a PEM fuel cell system for the cathode-side fuel gas channel and the GDL is considered. Figure 5.1 shows a

schematic diagram of the two-dimensional half-cell model with two pin fins along the transverse section of the flow channel.

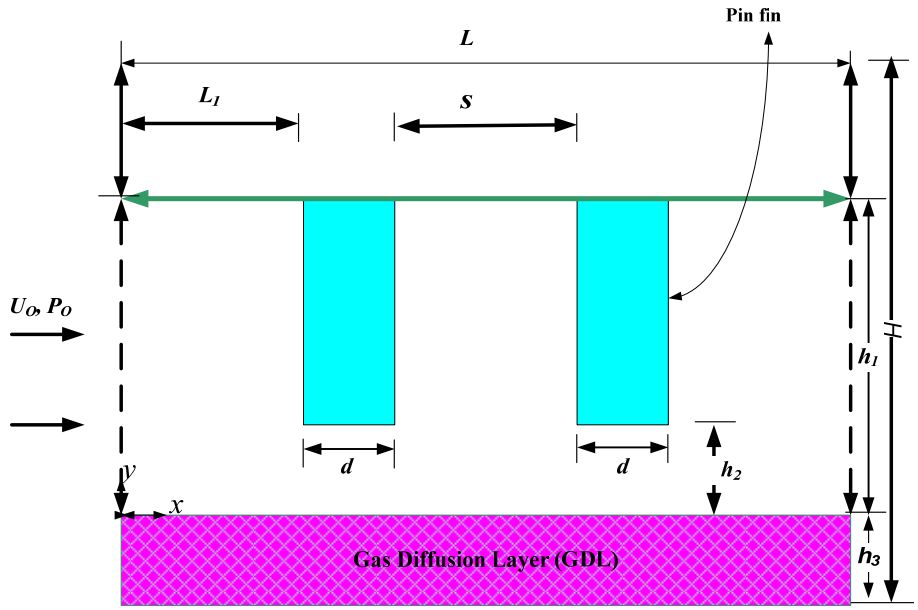

Figure 5.1 PEMFC half-cell model with two transverse pin fins along the flow channel

The fluid considered here is air at an inlet pressure, P_0, and velocity, U_0. The fin disturbance employed in this study protrudes from a rectangular base towards the GDL at a height to diameter ratio between 0.5 and 4. The parameters h_1, h_2 and h_3 (Figure 5.1) depict the flow channel height, tip clearance size and GDL thickness, respectively. The tip clearance size is characterised by defining a dimensionless parameter named, clearance ratio, $\lambda \equiv h_2/h_1$, for the study. The values of $\lambda = 0$ and 1 indicate fully blocked and block-free conditions, respectively, and the values in between are a measure of various levels of blockage [86]. Also defined, is another dimensionless parameter: the ratio of the distance between pin distances in the transverse direction to the fin thickness (pitch), $\zeta = s/d$. The effects of the tip clearance size, the pitch, the fuel flow Reynolds number (Re) and the porosity (ε) of

the GDL on the reactant gas transport, and the pressure drop across the channel are critically explored. The porosity, ε, of the porous medium is defined as the fraction of the total volume of the medium that is occupied by void space. In this study, parameters were varied in the following range: $0.2 \le \lambda \le 0.6$, $5.0 \le \zeta \le 10$, $50 \le Re \le 350$ and $0.2 \le \varepsilon \le 0.6$. Other parameters used for the modelled PEM fuel cell are shown in Table 5.1. The idea proposed in this chapter is aimed at improving the reactant species distribution over the catalyst layer in the fuel cells in order to increase the fuel cell performance at reduced pumping power requirement.

Table 5.1 Parameters of the modelled fuel cell

Channel length (mm)	120
Channel width (mm)	1.0
Channel depth (mm)	1.2
Membrane thickness (mm)	0.036
GDL thickness (mm)	0.21
Membrane porosity	0.5
Cell operating temperature (^{o}C)	70
Cell operating pressure (atm)	3
GDL permeability (m^2)	1.76×10^{-11}
Electric conductivity of GDL $(\Omega^{-1}m^{-1})$	300
Relative humidity	100%

5.2.1 GOVERNING EQUATIONS

The present chapter provides a two-dimensional solution for the half-cell model of a PEM fuel cell. The following assumptions are used in this study:

- the reactant gas (air) is an ideal gas, and the flow is incompressible steady and laminar;
- the GDL is from an isotropic porous material and uniform;

- the catalyst layer is treated as an ultra-thin layer (regarded as a boundary condition), hence the reactant gas is totally consumed in the reaction;
- the reaction is assumed to be fast, ensuring that the transport time scale is dominant when compared with the reaction time scale- this assumption allows treating the chemical reaction simply as a boundary condition at the catalyst layer; and
- the fuel cell operates at a constant temperature.

Based on these assumptions, the following governing equations for the gas channel and the GDL can be written as [147]:

In the gas channel section, the governing equations are:

$$\frac{\partial u}{\partial x}+\frac{\partial v}{\partial y}=0, \tag{5.1}$$

$$u\frac{\partial u}{\partial x}+v\frac{\partial u}{\partial y}=-\frac{1}{\rho}\frac{\partial P}{\partial x}+\nu\left(\frac{\partial^2 u}{\partial x^2}+\frac{\partial^2 u}{\partial y^2}\right), \tag{5.2}$$

$$u\frac{\partial v}{\partial x}+v\frac{\partial v}{\partial y}=-\frac{1}{\rho}\frac{\partial P}{\partial y}+\nu\left(\frac{\partial^2 v}{\partial x^2}+\frac{\partial^2 v}{\partial y^2}\right), \quad \text{and} \tag{5.3}$$

$$u\frac{\partial W_i}{\partial x}+v\frac{\partial W_i}{\partial y}=D_i\left(\frac{\partial^2 W_i}{\partial x^2}+\frac{\partial^2 W_i}{\partial y^2}\right), \tag{5.4}$$

where D_i and W_i depict the diffusivity and mass fraction of the species, respectively.

In the GDL section, the governing equations are:

$$\frac{\partial u}{\partial x}+\frac{\partial v}{\partial y}=0, \tag{5.5}$$

$$\varepsilon\left(u\frac{\partial u}{\partial x}+v\frac{\partial u}{\partial y}\right)=-\frac{\varepsilon}{\rho}\frac{\partial P}{\partial x}+\upsilon\varepsilon\left(\frac{\partial^2 u}{\partial x^2}+\frac{\partial^2 u}{\partial y^2}\right)-\frac{\upsilon\varepsilon^2}{k}u-\frac{\varepsilon^3 C_F\rho u}{\sqrt{k}}\sqrt{u^2+v^2}\ , \tag{5.6}$$

$$\varepsilon\left(u\frac{\partial v}{\partial x}+v\frac{\partial v}{\partial y}\right)=-\frac{\varepsilon}{\rho}\frac{\partial P}{\partial y}+\upsilon\varepsilon\left(\frac{\partial^2 v}{\partial x^2}+\frac{\partial^2 v}{\partial y^2}\right)-\frac{\upsilon\varepsilon^2}{k}v-\frac{\varepsilon^3 C_F\rho v}{\sqrt{k}}\sqrt{u^2+v^2} \tag{5.7}$$

and,

$$\varepsilon\left(u\frac{\partial W_i}{\partial x}+v\frac{\partial W_i}{\partial y}\right)=D_{i,eff}\left(\frac{\partial^2 W_i}{\partial x^2}+\frac{\partial^2 W_i}{\partial y^2}\right). \tag{5.8}$$

C_F in Eqs. (5.6) and (5.7) depicts the quadratic drag factor. The Blake-Kozeny correlation [86] is used for the relationship between the porosity and permeability, *k, of* the GDL:

$$k=\left(\frac{D_d^2}{150}\right)\left[\frac{\varepsilon^3}{(1-\varepsilon)^2}\right]\ , \tag{5.9}$$

where

$$D_d\equiv\frac{6V_d'}{S_d'}\ . \tag{5.10}$$

The last two terms in Eqs. (5.6) and (5.7) are drag force terms, added due to the presence of the porous wall, which might increase the pressure drop. The porous diffusion layer quantity is represented by the subscript *d* and V_d'/V_s' is a geometrical parameter which depicts the volume-to-surface ratio of the GDL [86]. In fuel cells, the fluid flow diffuses through the GDL for the reaction to take place on the MEA. The effective diffusivity $(D_{i,eff})$ for gas-phase flow in porous media can be written as:

$$D_{i,eff} = D\frac{\varepsilon}{\tau} \tag{5.11}$$

The porosity, ε, is the void volume fraction in the porous media. The tortuosity, τ, is a measure of the average path length of the species flow through the porous media compared to the linear path length in the direction of the species transport. The quantity (tortuosity) is usually estimated through experiment. Therefore, it is conventionally correlated in fuel cell studies using the Bruggeman correlation. This correlation assumes τ is proportional to $\varepsilon^{-0.5}$, resulting in the simpler expression [191]:

$$D_{i,eff} = D\varepsilon^{1.5}. \tag{5.12}$$

The porosity correlation is used to account for geometric constraints of the porous media.

The Reynolds number was defined as [205]:

$$\mathrm{Re} = \dot{m}D_{ch}/(\mu A_{ch}). \tag{5.13}$$

For hydraulic performance in the channel, an apparent friction factor, f, was evaluated by using the following equation [205]:

$$f = (\Delta P / L)D_{ch}/(\rho w^2/2), \tag{5.14}$$

where

$$w = \dot{m}/(\rho A_{ch}). \tag{5.15}$$

The channel flow resistance, $(\Delta P/\dot{m})$, is defined as [206]:

$$R_f = 2Po\nu L/D_{ch}^2 A_{ch}, \tag{5.16}$$

where Po is the Poiseuille constant.

The pumping power is evaluated by using the relation:

$$P_{pump} = \int_0^L \left[\frac{dp(x)}{dx} Q(x) \right] dx . \tag{5.17}$$

The water formation and transport of liquid water are modelled using a saturation model based on [72, 187]. In this approach, the liquid water formation and transport are governed by the conservation equation for the volume fraction of liquid water, s_w, or the water saturation [163]:

$$\frac{\partial(\varepsilon \rho_l s_w)}{\partial t} + \nabla \cdot (\rho_l \vec{V}_l s) = r_w, \tag{5.18}$$

where subscript l represents liquid water, and r_w is the condensation rate modelled as:

$$r_w = c_r \max\left(\left[(1 - s_w) \frac{P_{wv} - P_{sat}}{RT} M_{w,H_2O} \right], [-s_w \rho_l] \right) , \tag{5.19}$$

where r_w is added to the water vapour equation. The condensation rate is constant at $c_r = 100 s^{-1}$.

The clogging of the porous media and the flooding of the reaction surface are modelled by multiplying the porosity and the active surface area by $(1 - s_w)$, respectively.

5.2.2 NUMERICAL PROCEDURE

The model equations were solved using a finite-volume computational fluid dynamics code Fluent [163] with Gambit® (2.4.6) as a pre-processor. The CFD code has an add-on package for fuel cells, which has the requirements for the source terms for species transport equations, heat sources and liquid water formations. The domain was discretised using a second-order discretisation scheme. The pressure-velocity coupling was performed with the SIMPLE algorithm [192] for convection-diffusion analysis. Numerical convergence was obtained at each test condition when the ratio of the residual source (mass, momentum and species) to the maximum flux across a control surface was less than 10^{-6}.

Uniform isothermal free stream and fully developed fluid (air) with constant properties were assumed at the inlet and flows were fully developed at the outlet of the channel. At the interface between the gas channel and the GDL layer interface, the same velocity, the same concentration and the same gradients were imposed. No-slip no-penetration boundary conditions were enforced on the pin fins and wall surfaces.

The domain was divided into hexahedral volume elements. A grid independence test was carried out to ensure that solutions were independent of the dimensions of the chosen grid, with consideration of both accuracy and economics. For this purpose, four grid systems at 37 × 27, 82 × 27, 120 × 60 and 150 × 80 were tested. For the case of Re = 350, $\lambda = 0.6$, $\zeta = 7.0$ and $\varepsilon = 0.5$, the maximum relative deviation for the skin friction between the 120 × 60 grid and the 150 × 80 grid was less than 3%. It was considered that the system of 120 × 60 was sufficient for the study as a trade-off between accuracy and cost of time. A typical grid network for the computational domain is shown in Figure 5.2. The model and solution were implemented using an Intel® Core(TM) 2Duo 3.00 GHz PC with 3.24 GB of DDRam.

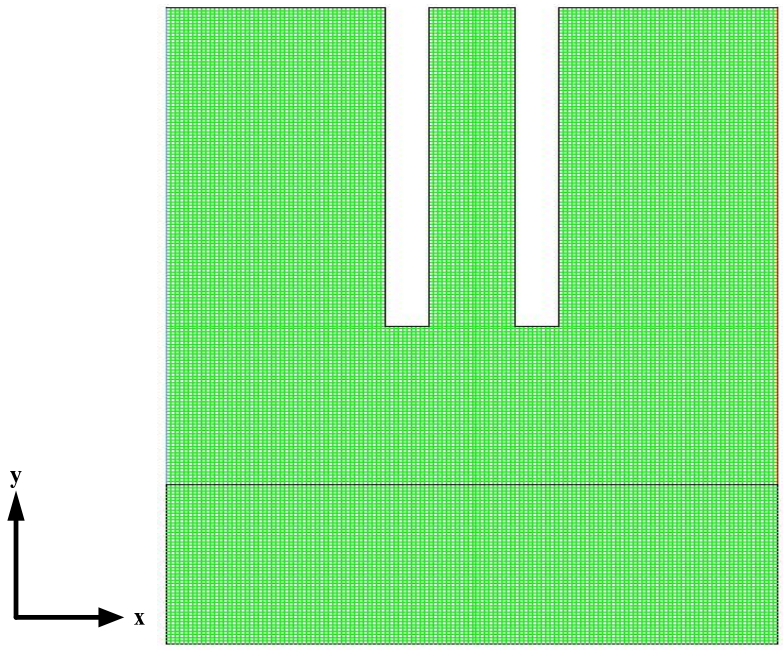

Figure 5.2 The representative grid system and computational domain

5.3 MATHEMATICAL OPTIMISATION ALGORITHM

The Dynamic-Q optimisation algorithm [166] previously discussed in Chapter 3 was used in this study. The algorithm is a robust multidimensional gradient-based optimisation algorithm which does not require an explicit line search and it is ideally robust for cases where the function evaluations are computationally expensive. The algorithm applies the dynamic trajectory LFOPC which is adapted to handle constrained problems through approximate penalty function formulation [166]. This dynamic approach is applied to successive quadratic approximations of the actual optimisation problem. The successive sub-problems are formed at successive design points by constructing spherically quadratic approximations, which are used to approximate the objective functions or constraints (or both) if they are not analytically given or very expensive to compute numerically [169, 207]. The use of spherically quadratic approximation in the Dynamic-Q algorithm offers a competitive advantage when compared with other algorithms in terms of computational and storage

requirements [169]. The storage savings become highly significant when the numbers of variables becomes large. Therefore, this particular strength of the Dynamic-Q method makes it well suited for optimisation of engineering problems with large numbers of variables and it has been used to successfully solve a large variety of engineering problems [207-213].

5.4 OPTIMISATION PROBLEM FORMULATION

The optimisation problem was tailored towards finding the best pin fin geometric parameters, which would give the maximum reactant species diffusion to the GDL of the fuel cell for a fixed Reynolds number, GDL thickness and GDL porosity at a reduced channel flow resistance, contributing to the increase in pressure drop along the channel. The apparent pressure drops increase the pumping power requirement for operating a fuel cell system. The design variables which greatly affect the hydrodynamic performance of pin fins are the geometric parameters s, d, h_2 and h_1 as depicted in the half-cell model shown in Figure 5.1.

The objective function for the optimisation can be written mathematically as,

$$I_{\max} = f(\lambda_{opt}, \varsigma_{opt}, \varepsilon_{opt}, Re_{opt}) \tag{5.20}$$

where $I_{\max}$ is the maximized current density output for the optimised design variables.

5.4.1 OPTIMISATION CONSTRAINTS

The optimisation problem was carried out subject to the following constraints:

5.4.1.1 *Total pin fin area constraint*

In pin fin application, the weight and material cost of pin fins are limiting factors. Hence, the total area of pin fins is fixed to a constant value:

$\therefore \sum A^c{}_j =$ Constant

$$\sum \pi D_j H_j = C \tag{5.21}$$

and

$$\sum D_j H_j = \frac{C}{\pi} \tag{5.22}$$

where $j = 1, 2$ and A^c is the pin fin area.

5.4.1.2 *The tip clearance size*

The tip clearance size, λ, is the ratio of the gap size between the pin fin tip and the GDL to the channel height. This was varied between 0.2 and 0.6:

$$0.2 \leq \left[\lambda = \frac{h_2}{h_1} \right] \leq 0.6. \tag{5.23}$$

5.4.1.3 *The pitch*

The pitch is the ratio of the distance between successive pin fins to the pin fin diameter. This was allowed to vary between 5 and 10:

$$5 \leq [\zeta = s/d] \leq 10\,. \tag{5.24}$$

5.4.1.4 *Manufacturing constraint*

The solid area fraction, φ, which is defined as the ratio of the pin fin material to the total area of the fuel cell channel was allowed to vary between 0.5 and 4. This is based on manufacturing and size constraints [214, 215]:

$$0.5 \le \left[\varphi = \frac{h_1 - h_2}{d} \right] \le 4. \tag{5.25}$$

Also, the interfin spacing is limited to 50 microns based on pin fin fabrication techniques [216, 217]:

$$s \ge 50\ \mu m. \tag{5.26}$$

5.4.2 OPTIMISATON PROCEDURE

The optimisation problem defined in Section 4.1 was solved by coupling the Dynamic-Q optimisation algorithm with CFD code FLUENT [163] and grid generation (GAMBIT [164]) code in a MATLAB [218] environment. Figure 5.3 depicts a flow diagram of how the automation was carried out until convergence (either by step size or function value criteria) was attained. To ensure that the converged solution obtained was indeed the global minimum, a multi-starting guess approach was employed.

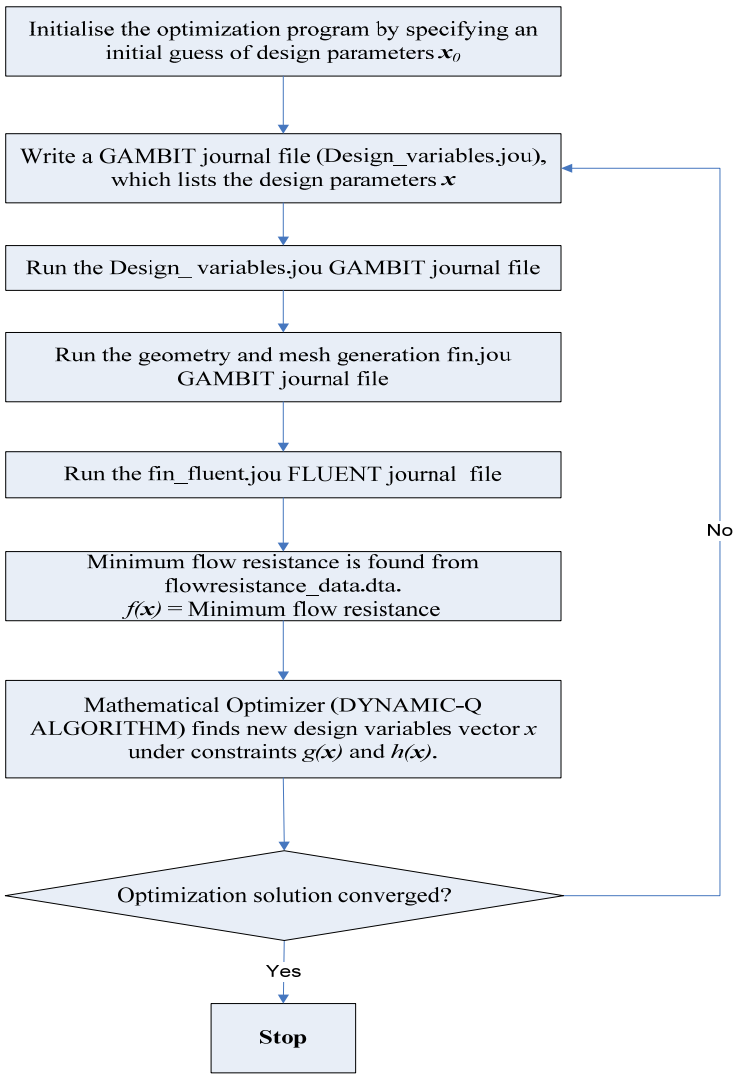

Figure 5.3 Optimisation automation flow diagram

5.5 RESULTS AND DISCUSSION

5.5.1 RESULTS OF FLOW FIELD

The pin fins employed in this work are expected to induce high levels of mixing of the main flow and/or the flow in the near-wall region and, subsequently, to improve the convection of reactant gas through the GDL. The power output in the fuel cell system is the consequence of the electrochemical reaction. Subsequently, the consumption of oxygen through diffusion into the catalyst membrane region is an index of the cell performance [78]. Higher oxygen mass flow rates through the GDL to the catalyst layer result in better fuel cell performance, since this reaction gas is more available to participate in the electrochemical reaction per unit of time. A qualitative description of the flow velocity pattern around the pin fin and within the GDL is presented in Figures 5.4-5.6 to illustrate the hydrodynamic phenomenon in the computational domain.

Figure 5.4 shows the Reynolds number influence on the flow pattern for the case of *s/d* = 5, and $\lambda = 0.2$ at a fixed GDL porosity of 0.5. The Reynolds number has a significant effect on the flow field and the diffusion of the reactant gas through the GDL medium. The rate of diffusion increases as the Reynolds number increases, thereby improving the reaction rate in the fuel cell system. The wake-shedding generated by the front pin fin interacts with the pin fin immediately behind it along the channel, which affects the flow-field characteristics. At a low Reynolds number of 50 (Figure 5.4a), there is flow attachment between the front pin and the back pin tips. This flow attachment also occurs at a Reynolds number of 150 (Figure 5.4b), but for a Reynolds number of 250 (Figure 5.4c), a flow separation occurs at the tip between the front pin and the back pin.

This increased Reynolds number creates the phenomenon of increasing the wake generation and the diffusion pattern into the GDL of the cell. The angle of separation of flow depends on the Reynolds number and the level of clearance ratio. As the clearance ratio increases, the location of the boundary layer separation moves forward. This movement is practically due to the change in the velocity distribution inside the boundary layer formed on the pin fins.

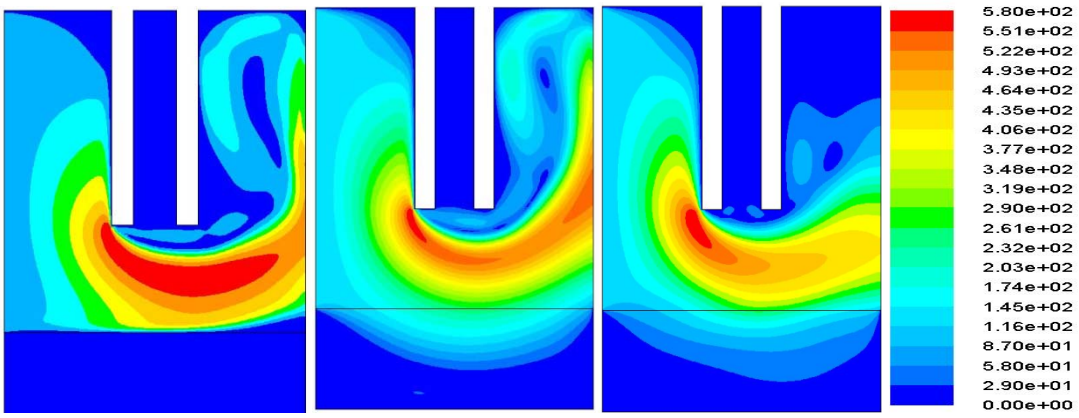

(a.) **(b.)** **(c.)**

Figure 5.4 Effect of Reynolds number on the flow field for different flow field configurations ($s/d = 5, \lambda = 0.2$): (a) Re = 50, (b) Re = 150, (c) Re = 250

The flow pattern for a higher tip clearance ($\lambda = 0.6$) is shown in Figure 5.5, where the effect of the Reynolds number (at fixed GDL porosity of 0.5) can also be clearly observed. The flow pattern in Figure 5.5 depicts the significant influence of the increase in the tip clearance between the pin fin and the GDL at the rate of reactant diffusion through the GDL into the catalyst reaction site.

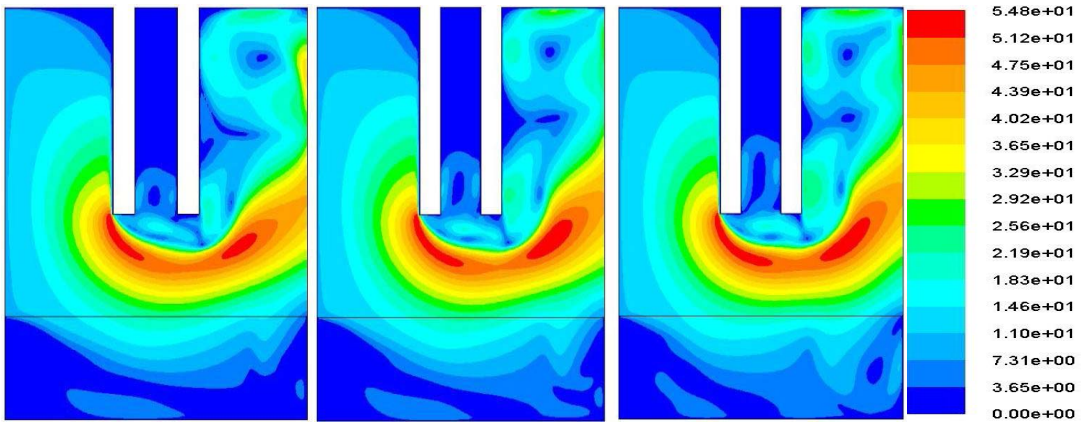

(a) **(b)** **(c)**

Figure 5.5 Effect of Reynolds number on the flow field for different flow field configurations ($s/d = 5, \lambda = 0.6$): (a) Re = 50, (b) Re = 150, (c) Re = 250

The reactant gases are forced down the GDL, hence improving the rate of electrochemical reaction for improved performance. In Figure 5.6, the contours of the tangential velocity profiles for the same case described in Figure 5.5 are shown. High pressure points are shown at the tips of the front pin. The rate of reactant gas diffusion into the GDL improves from Contours (a) to (c).

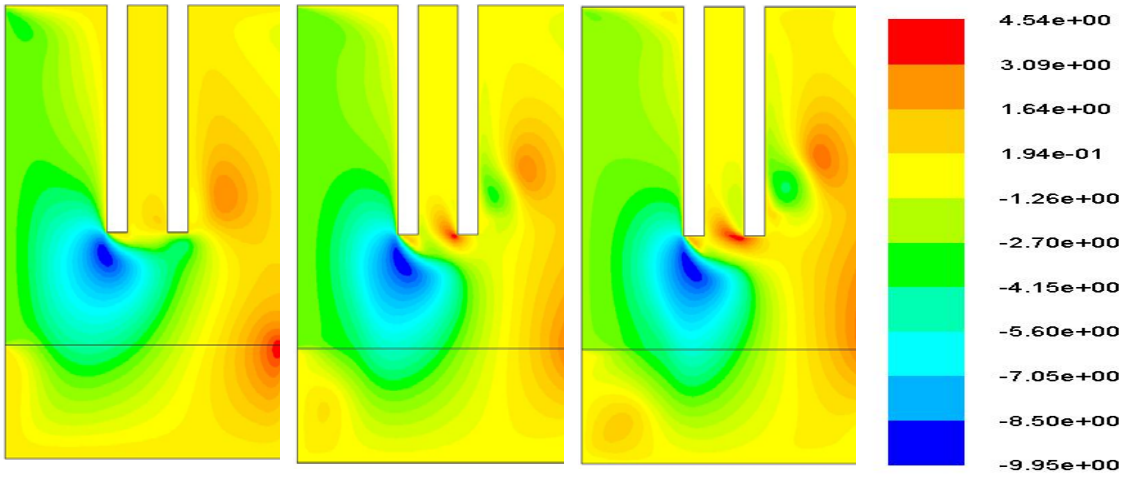

(a) (b) (c)

Figure 5.6 Contours of tangential velocity for different flow field configurations ($s/d = 5, \lambda = 0.6$): (a) Re = 50, (b) Re = 150, (c) Re = 250

5.5.2 RESULTS OF PIN FIN GEOMETRY

In Figure 5.7, we present the friction factor, *f,* as a function of the channels Reynolds number and the pitch (ratio of distance between the pin fin and the pin fin diameter). The friction factor decreased with the increasing Reynolds number. The data obtained in Figure 5.7 further shows that, as the pitch increases, the friction factor decreases. This implies lower diffusion of reactant gas, consequently reducing the performance of the fuel cell. Hence, lower pitch value, which generates more flow disturbance between the pin fin tip and GDL surface, will be more appropriate as this improves the fuel transport rate and subsequently, the reaction rate at the catalyst layer is improved. However, this should also be optimised for minimum power requirement.

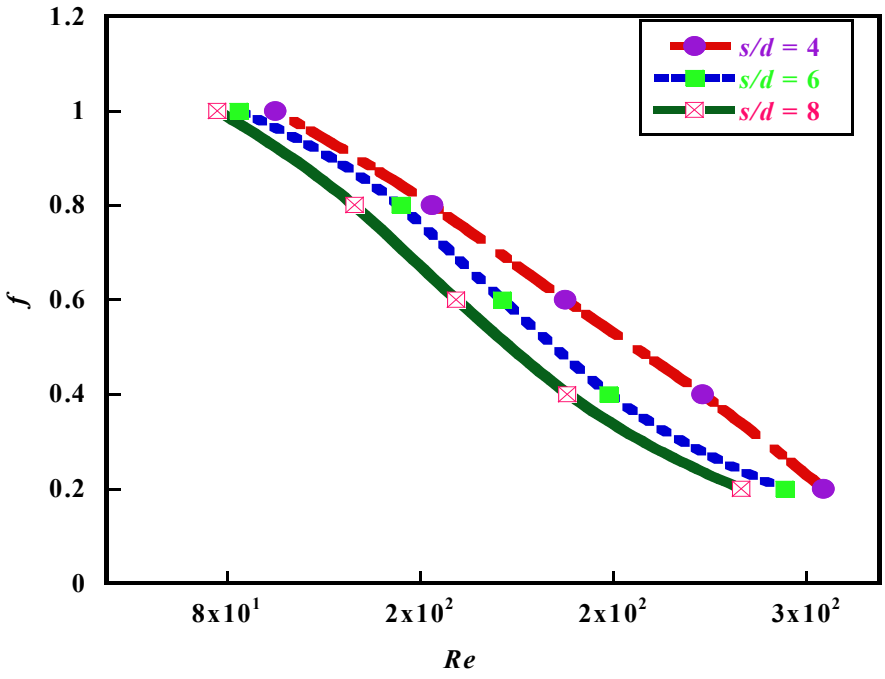

Figure 5.7 Fuel channel friction factor as a function of the Reynolds number and pitch at a clearance ratio, $\lambda = 0.3$

Figure 5.8 shows the variation of the friction factor as a function of the channel Reynolds number and the clearance ratio (λ) between the pin fin and the GDL surface. Decreasing λ, means that the height of the fin towards the GDL increases.

Similarly, decreasing the height of the pin fin reduces the pressure drop in the gas channel flow and subsequently reduces the convectional flow through the fuel cell GDL, thereby reducing cell performance. Increasing the height of the pin fin increases the fluid flow into the reaction site of the fuel cell. This is due to the tangential flow velocity created by the pin fin and flow-mixing effects, however, with a penalty of increasing the pumping power requirement due to increased pressure drop along the fuel channel. This is also supported by the flow description experienced at a higher λ in Figure 5.5. An optimised clearance ratio will reduce the associated pressure drop due to the increase in pin length towards the GDL and pumping cost will therefore decrease.

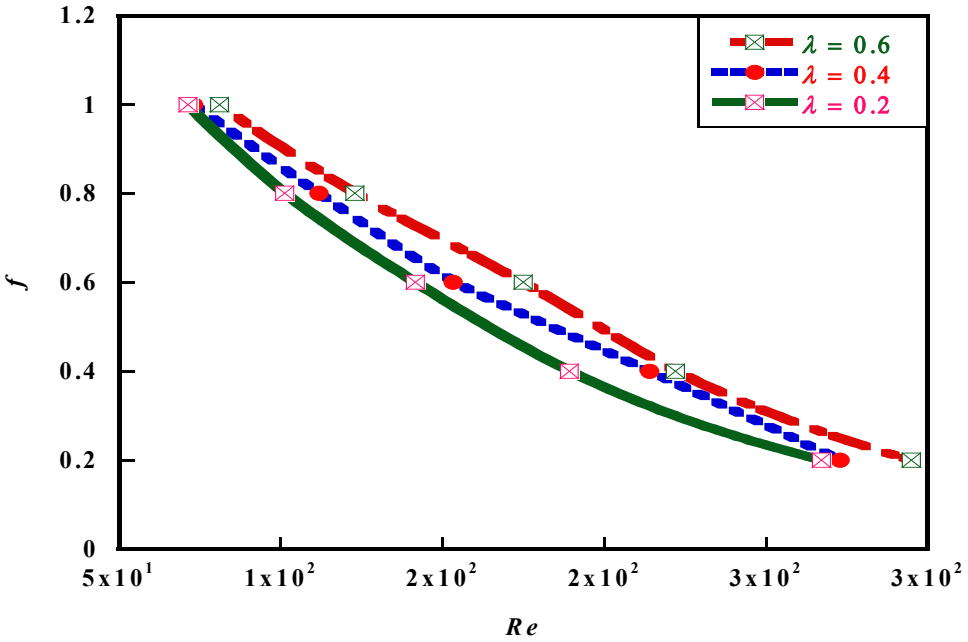

Figure 5.8 Fuel channel friction factor as a function of the Reynolds number and clearance ratio at a pitch, $s/d = 5$

Figure 5.9 depicts the friction factor as a function of channel Reynolds number and the GDL porosity. The results show a decrease in the friction factor with an increase in the GDL porosity of the fuel cell. The increased GDL porosity improves the convection flow through the GDL and subsequently improves fuel cell performance. The flow resistance in the channel at the larger GDL porosity (e.g. 0.7) is much less

than with the smaller porosity (e.g. 0.3). The pressure drop along the flow channel enhanced with pin fins can be reduced considerably with an appropriate higher GDL porosity.

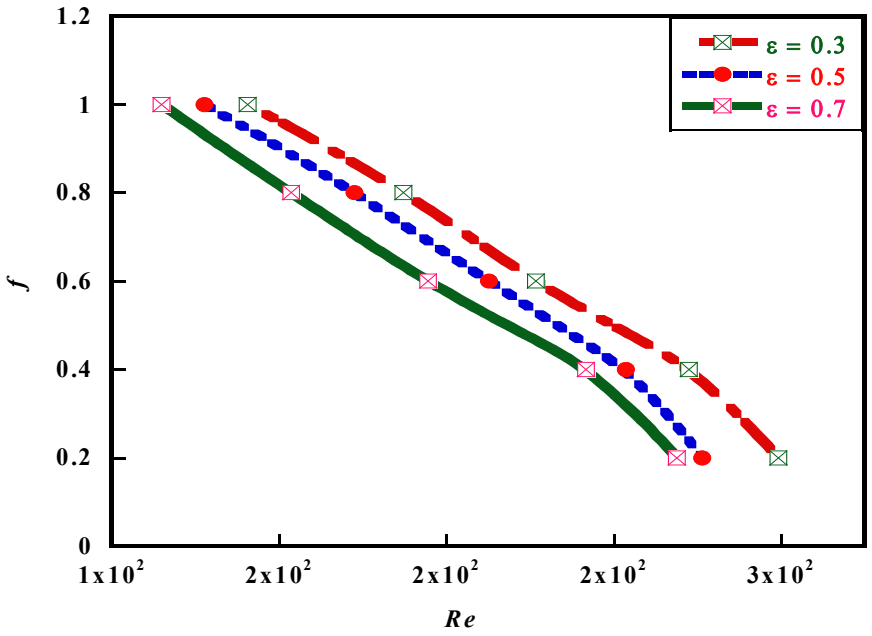

Figure 5.9 Fuel channel friction factor as a function of the Reynolds number and GDL porosity at a pitch, $s/d = 5$, and a clearance ratio, $\lambda = 0.3$

Figure 5.10 shows the peak channel flow resistance as a function of the clearance ratio and the GDL porosity. There is an optimum clearance ratio at $\lambda \approx 0.39$ in which the peak flow resistance in the fuel gas channel is minimised.

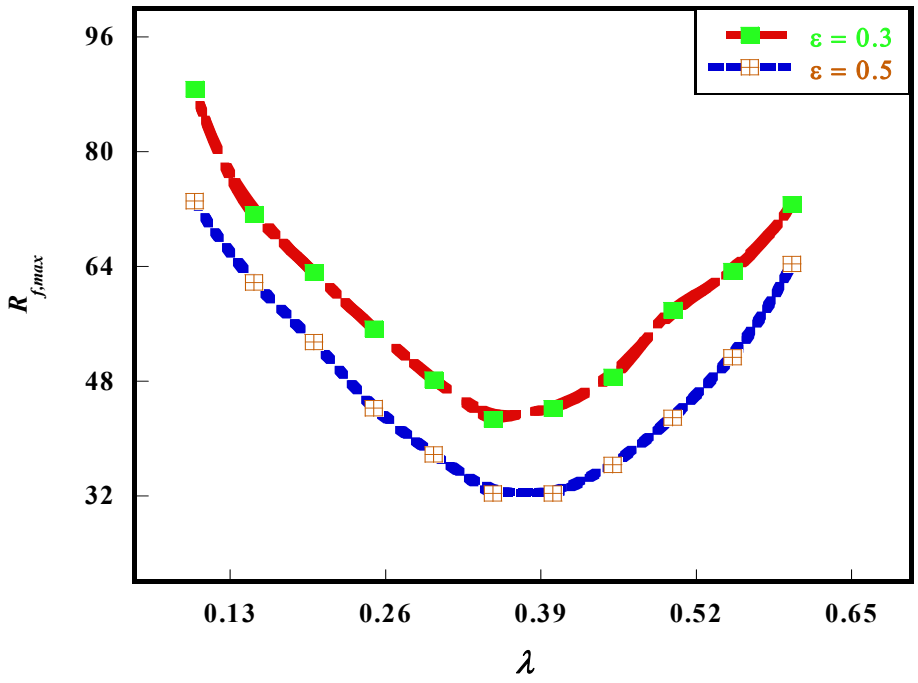

Figure 5.10 Effect of optimised clearance ratio on the peak channel flow resistance

Also, Figure 5.11 shows the peak channel flow resistance as a function of the pitch and the GDL porosity. There is also an optimal pitch at $s/d \approx 7.8$, which minimises the fuel channel friction. These results support the fact that an optimal arrangement of the pin fin parameters could effectively minimise the fuel channel friction and reduce the pressure drop along the fuel channel with a corresponding increase in reaction rate on the catalyst layer, thereby improving the fuel cell performance. Figures 5.10 and 5.11 also show that the GDL porosity has a significant effect on the peak flow resistance along the fuel gas channel. An increase in the GDL porosity reduces the peak flow resistance in the fuel channel. This observation is in agreement with previous work of Soong *et al.* [86].

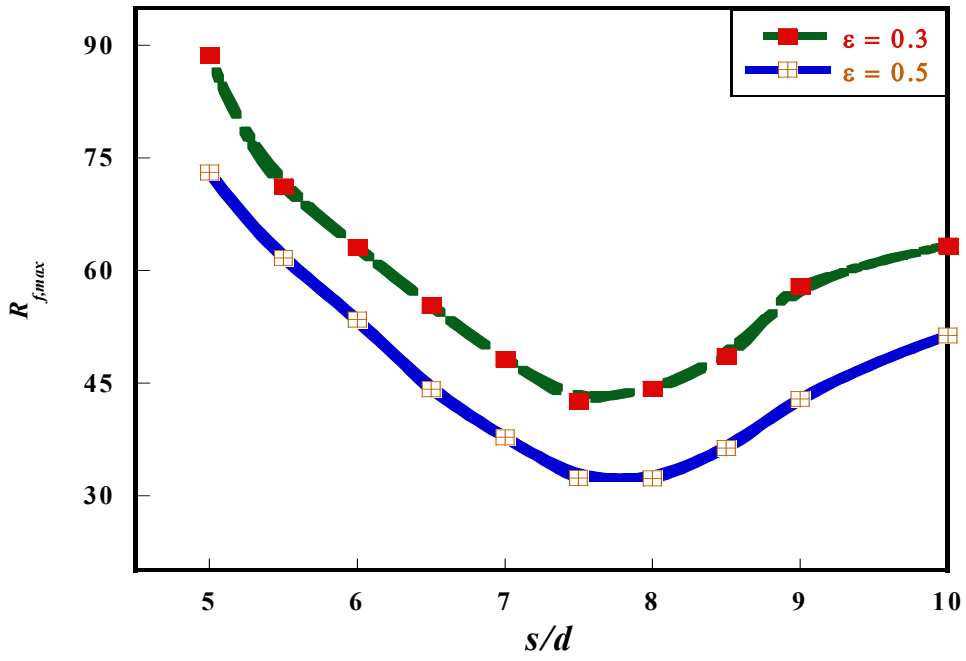

Figure 5.11 Effect of optimised pitch on the channel peak fuel channel flow resistance

5.5.3 OPTIMISATION RESULTS

In this section, the optimisation algorithm was applied to obtain the best geometric configuration of the pin fin that would offer optimal flow resistance along the fuel cell channel, thus ensuring optimum performance of the fuel cell system. From the results in Section 5.2, it is clear that the pin fin geometric parameters (clearance ratio and pitch) optimally exist, which minimises the channel flow resistance. This optimal geometric parameters and the porosity of the GDL have a significant influence on fuel cell performance through reactant gas distribution and the reaction rate on the catalyst layer. Reducing the inherent flow resistance along the flow channel will reduce the additional pressure drop, therefore reducing the pumping power requirement. A series of numerical optimisations and calculations were conducted within the design constraint ranges given in Section 4.1 and the results are presented in the succeeding section to highlight the optimal behaviour of the fuel cell system. Figure 5.12 shows

the effect of the minimised flow resistance as a function of the Reynolds number for a fixed clearance ratio of 0.3 and a GDL porosity of 0.5. Minimised flow resistance decreases with an increase in the Reynolds number.

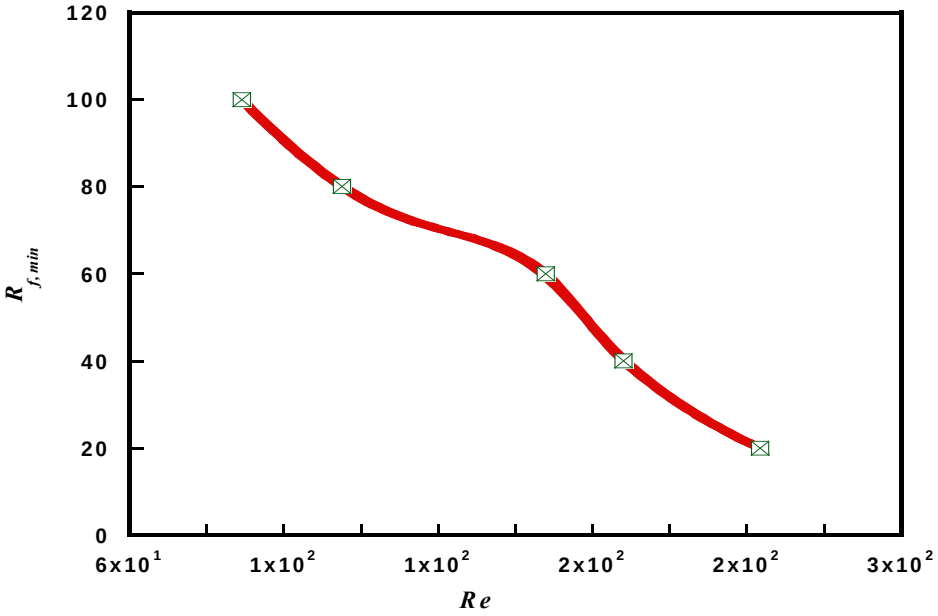

Figure 5.12 The minimised fuel channel flow resistance as a function of Reynolds number for a fixed GDL porosity, $\varepsilon = 0.5$, and a tip clearance ratio, $\lambda = 0.3$

Figure 5.13 shows that the optimal pin fin clearance ratio decreases as the Reynolds number increases. This result affirms the fact that a unique optimal pin fin clearance ratio exists for the fuel gas Reynolds numbers. Similarly, Figure 5.14 shows the optimal pitch as a function of the fuel gas Reynolds number at a fixed clearance ratio of 0.3 and a GDL porosity of 0.5. The result also shows the existence of a unique optimal pitch for the fuel gas Reynolds number.

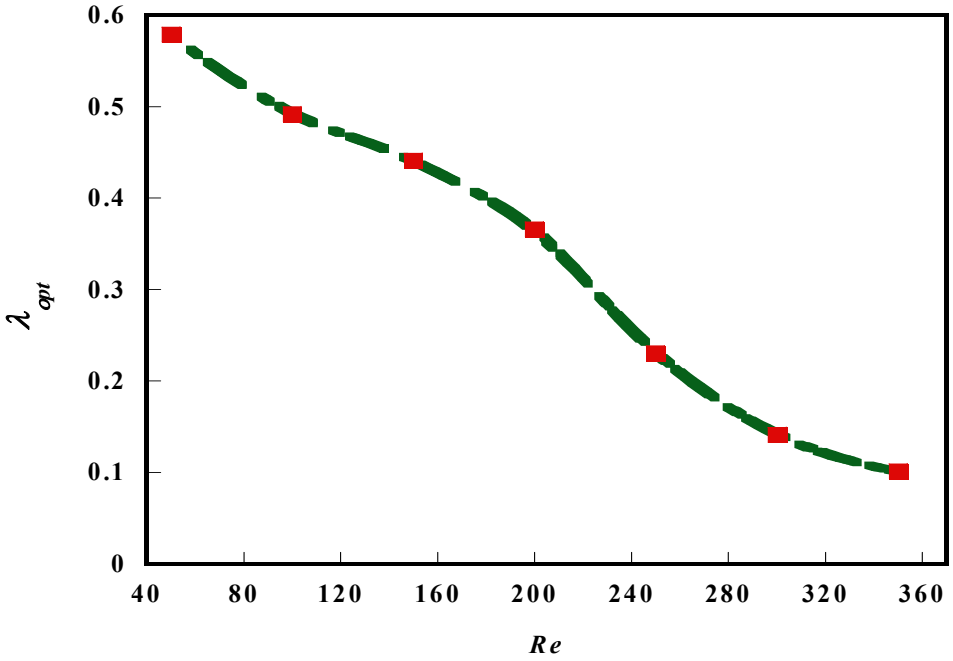

Figure 5.13 Optimal clearance ratio as a function of Reynolds number at a fixed pitch, $s/d = 5$, and a GDL porosity, $\varepsilon = 0.5$

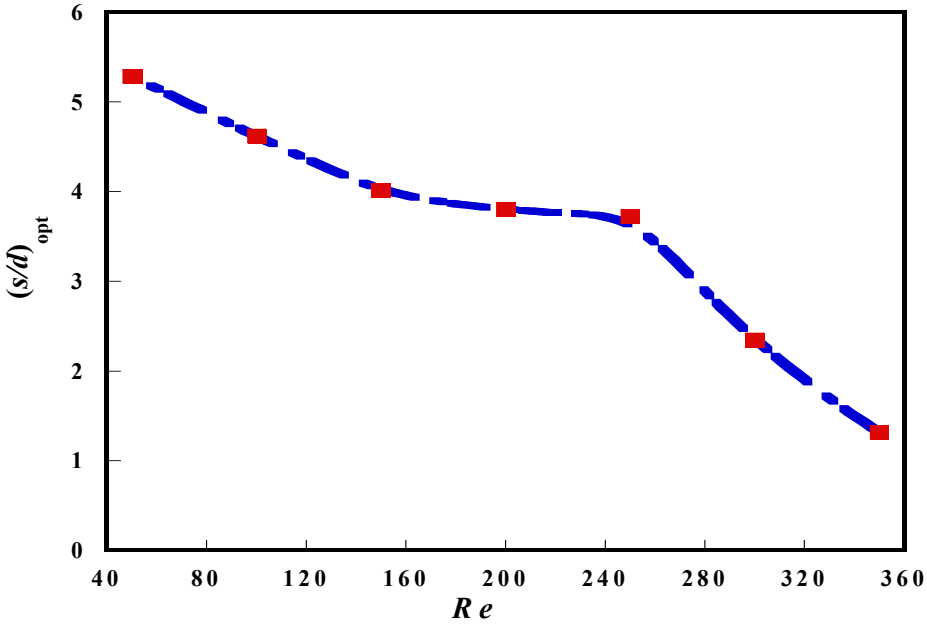

Figure 5.14 Optimal pitch as a function of Reynolds number at a fixed clearance ratio, $\lambda = 0.3$, and a GDL porosity, $\varepsilon = 0.5$

The effect of channel flow resistance on the optimised channel clearance ratio at a porosity of 0.5, pitch of 5 and Reynolds number of 250 was investigated in Figure 5.15. The result shows that channel flow resistance has a significant effect on the optimised clearance ratio. As the flow resistance increases, the optimal clearance ratio decreases.

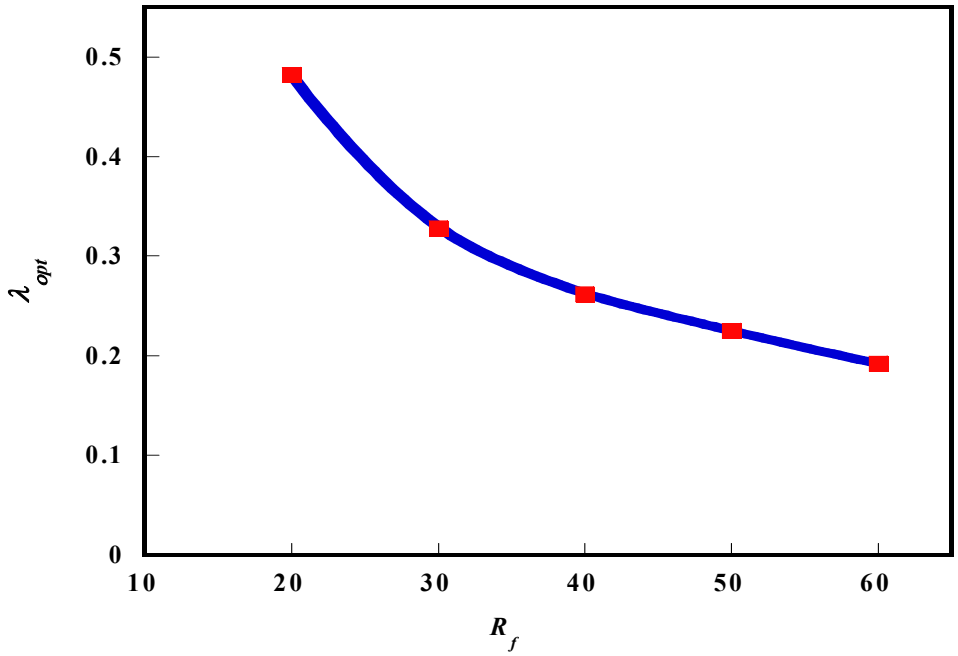

Figure 5.15 Effect of channel flow resistance on the optimised clearance ratio at a fixed pitch, $s/d = 5$, and a GDL porosity, $\varepsilon = 0.5$, at Reynolds number of 250

Also in Figure 5.16, the effect of channel flow resistance on the optimised pin fin pitch was investigated at a clearance ratio of 0.3, GDL porosity of 0.5 and Reynolds number of 250. The result shows that the optimised pitch decreases with an increase in channel flow resistance. Generally, in this model, the flow resistance decreases when the Reynolds number increases. The optimal clearance ratio and pitch also decrease with increasing channel flow resistance, but an optimal level of these factors (clearance ratio and pitch) exists which minimises the flow resistance of reactant gases in the fuel cell gas channel.

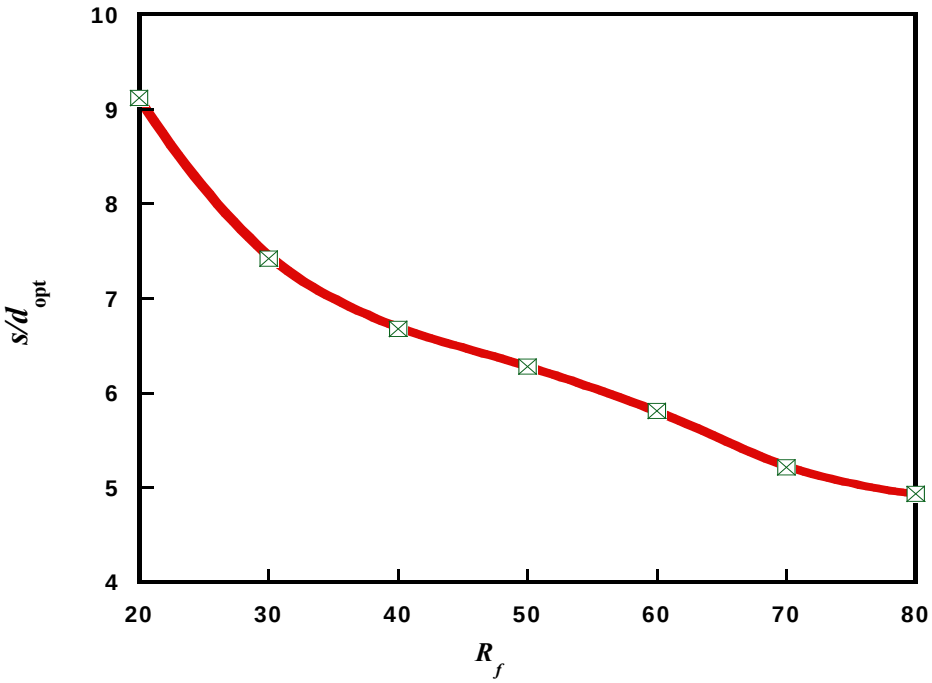

Figure 5.16 Effect of channel flow resistance on the optimised pitch at a fixed clearance ratio, $\lambda = 0.3$, and a GDL porosity, $\varepsilon = 0.5$, at a Reynolds number of 250

5.5.4 PERFORMANCE EVALUATION

Generally, in heat transfer studies using pin fins for enhancement, performance analysis is done by using performance evaluation criteria [203, 219]. Therefore, it is necessary to perform a similar analysis for this study and state the performance in terms of pressure drop for a fuel cell channel equipped with pin fins and one without pin fins. Figure 5.17 shows the pressure drop characteristic for a fuel cell channel with and without pin fins. As can be expected, the figure shows that higher pressure drops occur in the fuel channel with pin fins than in the fuel channel without pin fins. However, the difference obtained along the flow channel for all the pin fin geometry cases considered in this study was less than 6%.

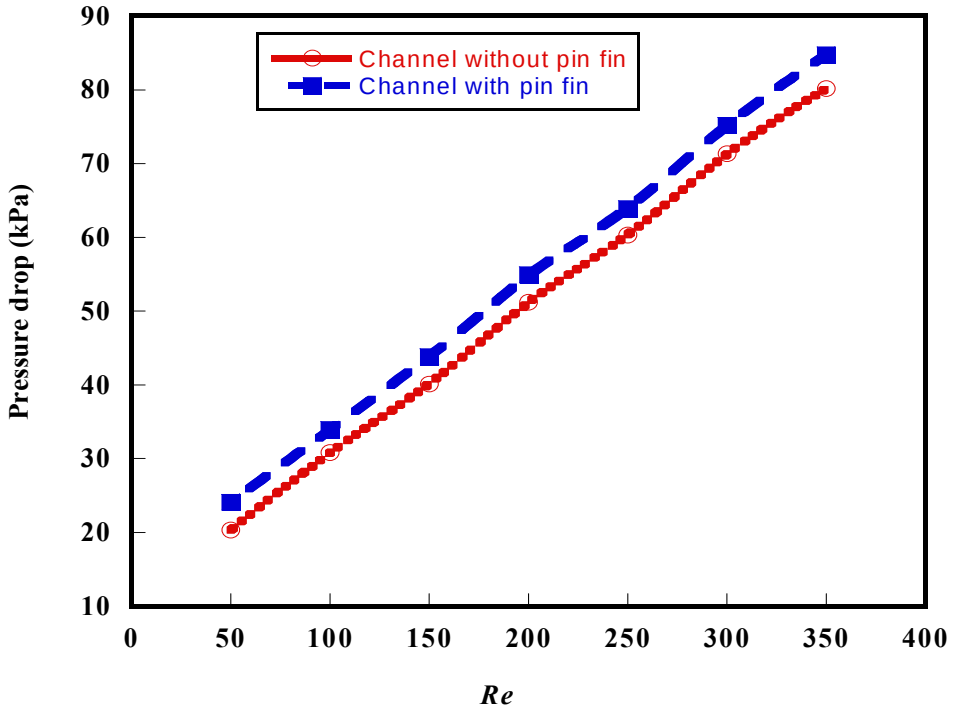

Figure 5.17 Fuel channel pressure drop as a function of the applied pressure drop for a channel with pin fin ($s/d = 5, \lambda = 0.3$) and one without pin fin

Thus, it is evident from this study that, in terms of both high performance enhancement and reasonable pressure drop in a fuel cell system, the pin-fin-enhanced fuel channel is a promising approach for the optimal design of a fuel cell system. Figure 5.18 shows the pumping power as a function of the clearance ratio at a Reynolds number of 250 for a pitch of 5 and GDL porosity of 0.6. The pumping power is the product of the volumetric flow rate and pressure drop. The result shows a minimum pumping power for the friction factor of the fuel channel at a fixed Reynolds number and a specified pitch and GDL porosity of the fuel cell system. In general, the clearance ratio, λ, which has a significant effect on the fuel gas flow, can be optimised to improve fuel cell performance at a reduced pumping power requirement.

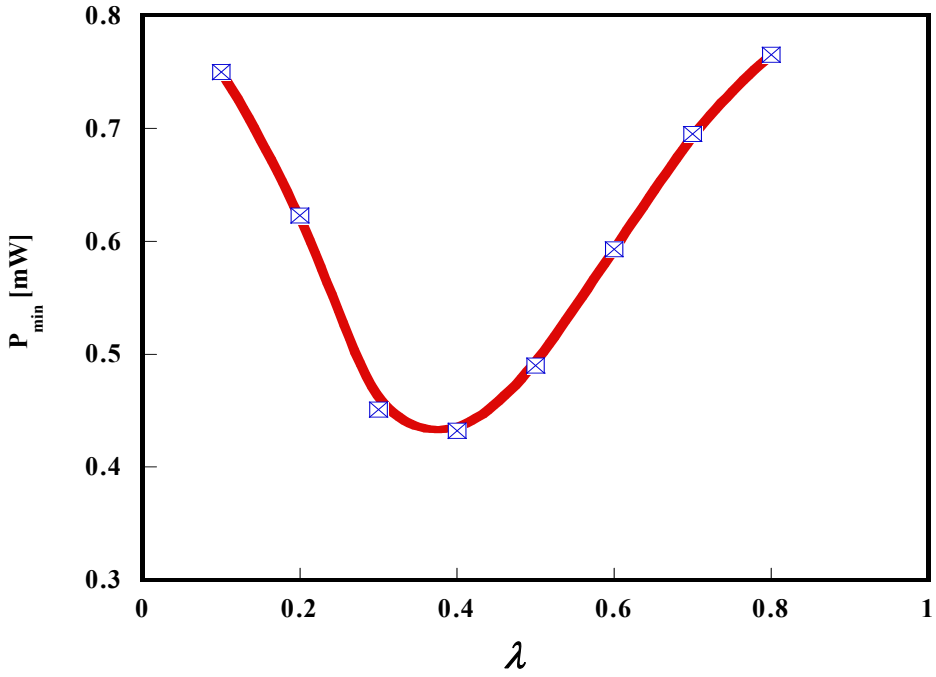

Figure 5.18 Pumping power as a function of tip clearance ratio at a pitch, *s/d* = 5, and GDL porosity, ε = 0.6, at a Reynolds number of 250

CONCLUSION

Using the numerical approach, the reactant gas transport phenomenon in the gas flow channel of a half-cell model of a PEM fuel cell with pin fin insert was investigated. The effect of the flow and geometrical parameters of the pin fin on the flow distribution in the GDL, as well as friction characteristics in the channel were critically studied. Pumping power requirements at varying pin fin clearance ratios to evaluate performance was also explored. The conclusions are summarised as:

- The flow Reynolds number had a significant effect on the reactant flow field, and the diffusion of the reactant gas through the GDL medium increased as the Reynolds number increased.

- The friction factor increased with an increasing clearance ratio of the pin fin in the channel.
- The optimal clearance ratio and pitch for the considered fuel cell channel decreased with an increase in the fuel channel friction.
- The friction factor decreased with an increase in the GDL porosity. Hence, the channel friction and pressure drop can be reduced significantly with increased GDL porosity.
- An optimal pin fin clearance ratio existed which offered minimum pumping power requirement.
- An enhanced fuel cell performance was achieved by using pin fins in a fuel cell gas channel, which ensured high performance and low fuel channel pressure drop of the fuel cell system.